

UV Luminosity Density Results at $z > 8$ from the First *JWST*/NIRCam Fields: Limitations of Early Data Sets and the Need for Spectroscopy

Rychard Bouwens^{1*}, Garth Illingworth², Pascal Oesch^{3,4}, Mauro Stefanon^{5,6}, Rohan Naidu^{7,8}, Ivana van Leeuwen¹, Dan Magee²

¹*Leiden Observatory, Leiden University, NL-2300 RA Leiden, Netherlands*

²*UCO/Lick Observatory, University of California, Santa Cruz, CA 95064*

³*Cosmic Dawn Center (DAWN), Niels Bohr Institute, University of Copenhagen, Jagtvej 128, København N, DK-2200, Denmark*

⁴*Department of Astronomy, University of Geneva, Chemin Pegasi 51, 1290 Versoix, Switzerland*

⁵*Departament d'Astronomia i Astrofísica, Universitat de València, C. Dr. Moliner 50, E-46100 Burjassot, València, Spain*

⁶*Unidad Asociada CSIC "Grupo de Astrofísica Extragaláctica y Cosmología" (Instituto de Física de Cantabria - Universitat de València)*

⁷*Center for Astrophysics, Harvard & Smithsonian, 60 Garden Street, Cambridge, MA 02138, USA*

⁸*MIT Kavli Institute for Astrophysics and Space Research, 77 Massachusetts Ave., Cambridge, MA 02139, USA*

Accepted XXX. Received YYY; in original form ZZZ

ABSTRACT

We have derived luminosity functions, and set constraints on the UV luminosity and SFR density from $z \sim 17$ to $z \sim 8$, using the three most-studied *JWST*/NIRCam data sets, the SMACS0723, GLASS Parallel, and CEERS fields. We first used our own selections on two independent reductions of these datasets using the latest calibrations. 18 $z \sim 8$, 12 $z \sim 10$, 5 $z \sim 13$, and 1 $z \sim 17$ candidate galaxies are identified over these fields in our primary reductions, with a similar number of candidates in our secondary reductions. We then use these two reductions, applying a quantitative discriminator, to segregate the full set of $z \geq 8$ candidates reported over these fields from the literature, into three different samples, “robust,” “solid,” and “possible”. Using all of these samples we then derive UV LF and luminosity density results at $z \geq 8$, finding substantial differences. For example, including the full set of “solid” and “possible” $z \geq 12$ candidates from the literature, we find UV luminosity densities which are $\sim 7\times$ and $\sim 20\times$ higher than relying on the “robust” candidates alone. These results indicate the evolution of the UV LF and luminosity densities at $z \geq 8$ is still extremely uncertain, emphasizing the need for spectroscopy and deeper NIRCam+optical imaging to obtain reliable results. Nonetheless, even with the very conservative “robust” approach to selections, both from our own and those of other studies, we find the luminosity density from luminous ($M_{UV} < -19$) galaxies to be $\sim 2\times$ larger than is easily achievable using constant star-formation efficiency models, similar to what other early *JWST* results have suggested.

Key words: galaxies: evolution – galaxies: high-redshift – dark ages, reionization, first stars

1 INTRODUCTION

One particularly interesting long-standing question in extragalactic astronomy has been “how early did massive galaxies begun to assemble?”. While this question had been the subject of many investigation prior to the start of *James Webb Space Telescope* (*JWST*) operations (Rigby et al. 2022), with inferences being made both using very high redshift luminosity functions (e.g., Bouwens et al. 2016, 2019, 2022a; Oesch et al. 2018; Stefanon et al. 2019; Bowler et al. 2020) and leveraging constraints on the stellar mass in sources (e.g., Duncan et al. 2014; Grazian et al. 2015; Song et al. 2016; Bhatawdekar et al. 2019; Kikuchi et al. 2020; Furtak et al. 2021; Stefanon et al. 2021, 2022a), early *JWST* investigations are already demonstrating the revolutionary potential of *JWST* for addressing the early galaxy assembly timescale (e.g. Adams et al. 2022; Naidu et al. 2022a; Castellano et al. 2022; Donnan et al. 2022; Atek et al. 2022; Finkel-

stein et al. 2022c; Harikane et al. 2022b; Bouwens et al. 2022b; Robertson et al. 2022).

These early studies have have returned very luminous and seemingly robust sources at $z \sim 10$ –13 (e.g. Naidu et al. 2022a; Castellano et al. 2022; Finkelstein et al. 2022a; Bouwens et al. 2022b), and have also identified candidates out to redshifts as high as $z \sim 16$ –20 (e.g. Donnan et al. 2022; Atek et al. 2022; Harikane et al. 2022a; Naidu et al. 2022b; Zavala et al. 2022; Yan et al. 2022; Finkelstein et al. 2022b). At the same time, some very massive sources have been identified at $z \geq 7$ on the basis of what appear to be substantial Balmer breaks (Labbé et al. 2022), suggesting substantial early mass assembly in the universe. These results are enigmatic, however, potentially exceeding the available baryons to form stars at $z \geq 13$ (Boylan-Kolchin 2022; Naidu et al. 2022b, but see also Steinhart et al. 2022; Inayoshi et al. 2022; Harikane et al. 2022a).

Despite this flurry of new high-redshift sources, there have been substantial differences in the $z \geq 8$ candidate galaxy samples identified in different studies over the same fields. The typical overlap between candidate lists in the earliest analyses were only ~ 10 –20% (at

* email: bouwens@strw.leidenuniv.nl

least in the initial versions of these papers).¹ Broadly such differences can be indicative either of substantial contamination in $z \geq 8$ selections or high levels of incompleteness.² In either case, the inferred luminosity function results could be substantially mis-estimated (by ~ 0.3 - 0.5 dex). Overall, this entire issue poses a major challenge as we try to understand what is really happening in the first 400-500 Myr at $z \geq 10$ where *JWST* can provide unique new insights into galaxy buildup.

The primary purpose of the present paper is to investigate the evolution of the UV luminosity density and star formation rate density for galaxies at $z \geq 8$ from early *JWST* data sets, while looking closely at the overall range of constraints allowed based on current observations. Key to doing this in a quantitative way is to provide an assessment of the first selections of $z \geq 8$ candidate galaxies over the first *JWST* data sets and any updates to these selections that have become possible due to improvements e.g. from improved zeropoint calibrations (e.g. Adams et al. 2022), and to identify approaches that lead to the most robust samples.

To this end, we will make use of two independent, recent reductions of the available *JWST* data that use the latest calibrations and experience in dealing with artifacts, over the three most well-studied fields, the SMACS0723 cluster (Pontoppidan et al. 2022), four NIRC-Cam pointings from the Cosmic Evolution Early Release Science (CEERS) fields (Finkelstein et al. 2022b), and the NIRC-Cam GLASS parallel field (Treu et al. 2022). Not only do we select our own set of $z \geq 8$ candidates from these fields, but we also make an assessment of essentially all candidates from previous studies of these same fields, to gauge how well individual selections appear to be working and to characterize potential progress. In doing so, we present community LF results, showing the impact of including candidates of various quality on the UV LF and luminosity density results at $z > 8$. We will also investigate the extent to which an emergent picture is forming on the basis of the latest results from the collective analyses.

The plan for this paper will be as follows. In §2, we summarize the data sets utilized in this paper and our procedure for performing photometry of sources in those data sets. In §3, we present our procedure for selecting $z \geq 7$ sources from the data sets we examine, the $z \sim 8$ -17 samples we derive, and our $z \sim 8$, 10, 13, and 17 LF results, while performing a detailed assessment of other candidate $z \sim 8$ -17 galaxies in the recent literature. In §4, we use those results to derive LF results based on our own selections and our community samples, discuss the results in §5, and then provide a summary in §6. For convenience, the *HST* F435W, F475W, F606W, F814W, F098M, F125W, F140W, and F160W filters are written as V_{606} , I_{814} , Y_{098} , J_{125} , H_{140} , and H_{160} , respectively, throughout this work. Also we quote results in terms of the approximate characteristic luminosity $L_{z=3}^*$ derived at $z \sim 3$ by Steidel et al. (1999), Reddy & Steidel (2009), and many other studies. A Chabrier (2003) initial mass function is assumed throughout. All magnitude measurements are given using the AB magnitude system (Oke & Gunn 1983) unless otherwise specified.

Table 1. Estimated 5σ depth [in mag] of the three *JWST* fields (SMACS0723, CEERS, and Abell 2744 parallel) we use in searching for galaxies at, nominally, $z \sim 8$, $z \sim 10$, $z \sim 13$, and $z \sim 17$. A $0.35''$ -diameter aperture is adopted for the photometry in computing the depth in each field.

Filter	5σ Depths (AB mag)		
	SMACS0723	GLASS-P	CEERS
<i>HST</i> /F435W	26.8	—	28.4
<i>HST</i> /F606W	27.6	28.6	28.6
<i>HST</i> /F775W	—	28.3	—
<i>HST</i> /F814W	27.2	—	28.4
<i>JWST</i> /F090W	28.7	28.9	—
<i>HST</i> /F105W	26.9	—	26.9
<i>JWST</i> /F115W	27.6	28.9	28.7
<i>HST</i> /F125W	26.2	—	26.8
<i>HST</i> /F140W	26.4	—	26.2
<i>HST</i> /F160W	26.4	—	27.2
<i>JWST</i> /F150W	29.1	28.9	28.9
<i>JWST</i> /F200W	29.3	29.0	29.2
<i>JWST</i> /F277W	29.5	29.3	29.0
<i>JWST</i> /F356W	29.4	29.2	28.9
<i>JWST</i> /F410M	—	—	28.1
<i>JWST</i> /F444W	29.1	29.5	28.4
Area [arcmin ²]	9.5	7.0	33.8

2 DATA SETS AND PHOTOMETRY

2.1 Data Sets

We make use of the three most studied NIRC-Cam data sets in constructing a selection of $z \geq 7$ galaxies from current *JWST* observations, i.e., the ~ 12 -hour SMACS0723 cluster field featured in the *JWST* early release observations (Pontoppidan et al. 2022), the 4-pointing NIRC-Cam observations taken as part of the CEERS early release science program (Finkelstein et al. 2022b), and the sensitive NIRC-Cam parallel observations as part of the GLASS early release science program (Treu et al. 2022).

These three fields cover a total area of ~ 51 arcmin². The approximate 5σ depths of these data sets reach from ~ 28 to 29.2 mag and are presented in detail in Table 1. These depths are derived by measuring the flux variations in source-free $0.35''$ -diameter apertures across our reduced images of each field.

We derived PSFs for the fields by taking a PSF from WebbPSF and then drizzling onto a grid consistent with our NIRC-Cam reductions. The FWHMs for the F090W, F115W, F150W, F200W, F277W, F356W, F410M, and F444W PSFs are $0.06''$, $0.06''$, $0.06''$, $0.07''$, $0.12''$, $0.14''$, $0.15''$, and $0.16''$, respectively. We also extracted empirical PSFs based on isolated, non-saturated stars located across the NIRC-Cam images and obtained consistent results.

Our fiducial reductions of each data set are executed using the GRIZLI software (Brammer et al. 2022). GRIZLI has procedures in place both to minimize the $1/f$ noise and to mask “snowballs” on individual NIRC-Cam frames. GRIZLI combines NIRC-Cam frames using the *astrodrizzle* software package, after modifying the headers of the frames to use the required SIP WCS headers. The GRIZLI reductions also take advantage of both significantly improved flat fields (and the jwst_0942.pmap calibration files) that became available in early September and the zeropoint adjustments derived by G. Brammer et al. (2022, in prep).

To better understand possible systematics and how they impact the selection of star-forming galaxies at $z \geq 6$, we also make use of the NIRC-Cam imaging pipeline PENCIL (Magee et al. 2022, in prep) built

¹ <https://twitter.com/stewilkins/status/1554909423759409153>

² For example, in cases where source selection is $\geq 80\%$ complete, different selections should overlap at $\geq 65\%$ level. Conversely, if source overlap between selections is less than 20%, then the completeness of individual selections cannot be generally higher than 50%.

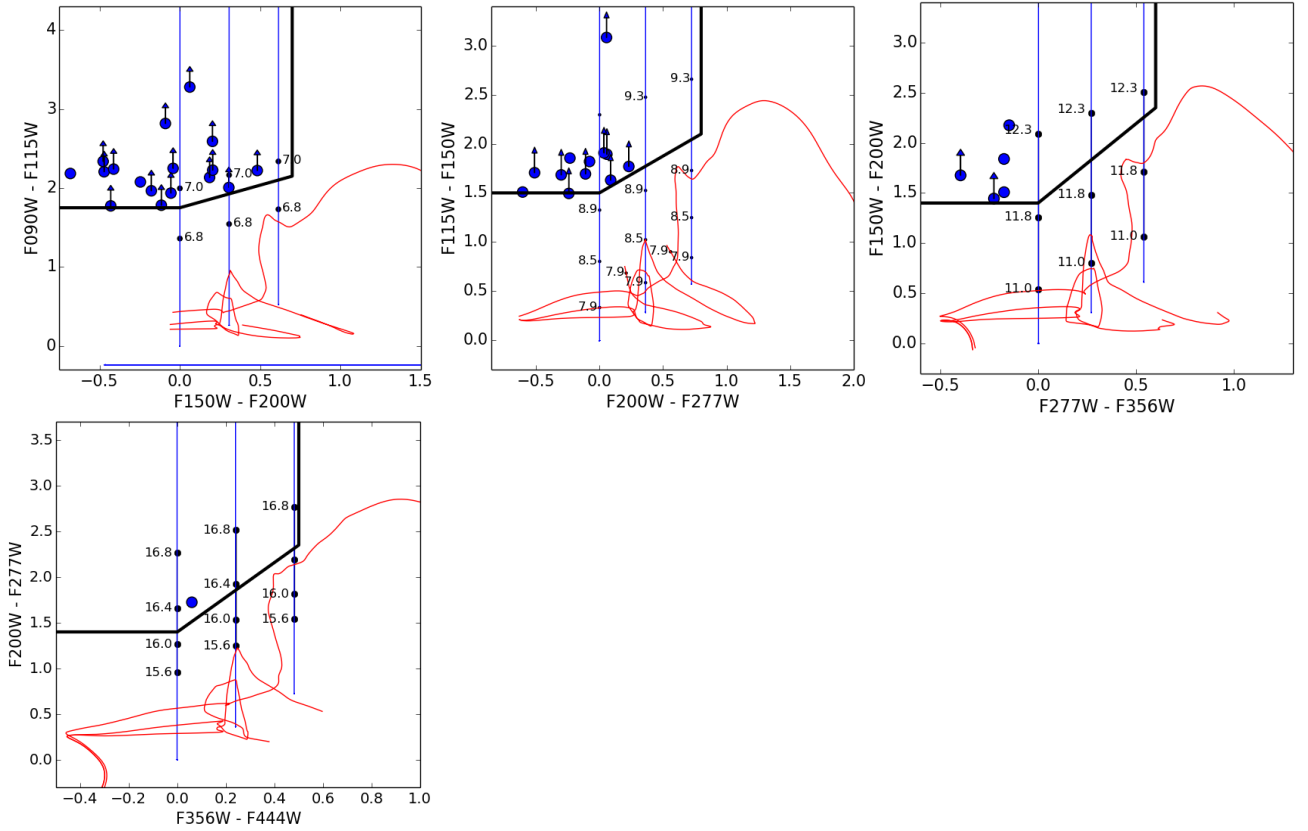


Figure 1. Two color Lyman-break selection criteria we use in identifying our nominal $z \sim 8$, $z \sim 10$, $z \sim 13$, and $z \sim 17$ candidate galaxies in three of the *JWST*/NIRCcam data sets that have been widely used for early galaxy selections. The thick black lines indicate the boundaries of our color-color criteria. The blue lines indicate the expected colors of star-forming galaxies with 100 Myr constant SF histories and $E(B - V)$ dust extinction of 0, 0.15, and 0.3, with colors at specific redshifts indicated by the black dots. The red lines show the expected colors of lower-redshift template galaxies from Coleman et al. (1980) out to $z \sim 5$. The solid blue circles show the colors of specific sources in our primary selection. In cases where sources are not detected in a band, they are shown with an arrow at the 1σ limit. These nominal selections span the redshift ranges $z \sim 7 - 9$, $z \sim 9 - 11$, $z \sim 12 - 14$ and $z \sim 16 - 19$, respectively (cf. Figure 2).

for the PRIMER team (PI: Dunlop). This pipeline leverages STScI’s *JWST* Calibration pipeline (v1.6.2), but also includes additional processing steps which are not part of the standard calibration pipeline. This includes the subtraction of $1/f$ noise striping patterns (both vertical and horizontal) that are not fully removed by the standard calibration pipeline and the subtraction of “wisps” artifacts from the short wavelength filters F150W and F200W in the NRCA3, NRCB3, and NRCB4 detector images.

Additionally, the background sky subtraction is performed by subtracting the median background over a $N \times N$ grid while using a segmentation map to mask pixels attributed to sources. Image alignment is executed in two passes using the calibration pipeline’s TWEAKREG step and then using STScI python package TWEAKWCS: the first pass uses TweakReg to group overlapping images for each detector/filter and perform an internal alignment within the detector/filter group; the second performs alignment against an external catalog using TweakWCS. The external catalog is, if possible, generated from an HST ACSWFC image mosaic which has been registered to the GAIA DR3 catalog.

Finally, the PENCIL reductions we utilize take advantage of calibration files (jwst_1009.pmap) which have been updated to reflect

new in-flight photometric zeropoints.³ Before the final NIRCcam image mosaics are generated using the calibration pipeline CALWEB_IMAGE3 stage, we perform an additional step to identify and mask “snowball” artifacts that are not identified and masked during the CALWEB_DETECTOR1 stage.

For the *HST* Advanced Camera for Surveys (ACS) and Wide Field Camera 3 near-IR (WFC3/IR) observations over SMACS0723, GLASS parallel field, and CEERS Extended Groth Strip (EGS) field, we made use of a reduction of the data generated by GRIZLI for our fiducial set of reductions made with GRIZLI. For the alternate set of reductions made with PENCIL, we used reductions made with ASTRODRIZZLE for the SMACS023 and GLASS parallel fields, following many of the same procedures used in the product of the XDF data set (Illingworth et al. 2013). Finally, for the CEERS EGS field, we made use of the ACS and WFC3/IR data products made available by CEERS team prior to the start of science observations by *JWST*.

2.2 Source Detection and Photometry

As in previous efforts by our team (e.g. Bouwens et al. 2011, 2015, 2019, 2021, 2022a), we perform source detection and photometry

³ <https://www.stsci.edu/contents/news/jwst/2022/an-improved-nircam-flux-calibration-is-now-available.html>

using SExtractor (Bertin & Arnouts 1996). For our F090W, F115W, F150W, and F200W dropout selections, source detection is performed using the square root of χ^2 image constructed by coadding PSF-matched F200W, F277W, F356W, and F444W data over the fields. PSF matching is done using our own implementation of the Lucy-Richardson deconvolution algorithm (Richardson 1972; Lucy 1974).

Color measurements for sources are made based on the measured flux in $0.35''$ -diameter apertures, after PSF-correcting the shorter wavelength data to match the PSF in the F444W band. These measurements are then corrected to total using (1) the additional flux in scalable Kron (1980) apertures with Kron factor of 2.5 and (2) using the estimated flux outside these scalable apertures based on the encircled energy distribution in the derived PSFs.

Finally, a foreground dust correction based on extinction maps of Schlafly & Finkbeiner (2011) is applied to colors and total magnitude measurements.

3 SOURCE SELECTIONS

3.1 Lyman Break Selections

We make use of two-color Lyman break selections to identify $z > 6$ galaxies from the *JWST* data of the three fields identified above. Lyman-break selections have been shown to be a very efficient way of identifying star-forming galaxies in the distant universe (e.g., Steidel et al. 1999; Bouwens et al. 2011, 2015, 2021; Schenker et al. 2013) and largely lie at the redshifts targeted by Lyman-break selections, given adequate S/N and bands either side of the break (e.g. Steidel et al. 1999, 2003; Stark et al. 2010; Ono et al. 2012; Finkelstein et al. 2013; Oesch et al. 2015; Zitrin et al. 2015; Oesch et al. 2016; Hashimoto et al. 2018; Jiang et al. 2021).

In devising color-color criteria for our selection, we follow the strategy employed in Bouwens et al. (2015, 2021) and make use of a two-color selection criterion, the first color probing the Lyman break and the second color probing the color of the *UV*-continuum just redward of the break. In choosing the passbands to utilize for this second color, we select bands which show no overlap with either the Lyman or Balmer breaks, ensuring that our selection would include even sources with prominent Balmer breaks, as Labbé et al. (2022) find at $z \sim 7$ -10.

After some experimentation, we made use of the following two color criteria:

$$(F_{090W} - F_{115W} > 1.75) \wedge (F_{150W} - F_{200W} < 0.7) \wedge \\ (F_{090W} - F_{115W} > 1.75 + 0.57(F_{150W} - F_{200W}))$$

for our nominal $z \sim 8$ selection,

$$(F_{115W} - F_{150W} > 1.5) \wedge (F_{200W} - F_{277W} < 0.8) \wedge \\ (F_{115W} - F_{150W} > 1.5 + 0.75(F_{150W} - F_{200W}))$$

for our nominal $z \sim 10$ selection,

$$(F_{150W} - F_{200W} > 1.4) \wedge (F_{277W} - F_{356W} < 0.8) \wedge \\ (F_{150W} - F_{200W} > 1.4 + 0.75(F_{277W} - F_{356W}))$$

for our nominal $z \sim 13$ selection, and

$$(F_{200W} - F_{277W} > 1.4) \wedge (F_{356W} - F_{444W} < 0.5) \wedge \\ (F_{200W} - F_{277W} > 1.4 + 1.58(F_{356W} - F_{444W}))$$

for our nominal $z \sim 17$ selection. In cases where sources are undetected in a given band, flux is set to the 1σ limit when applying

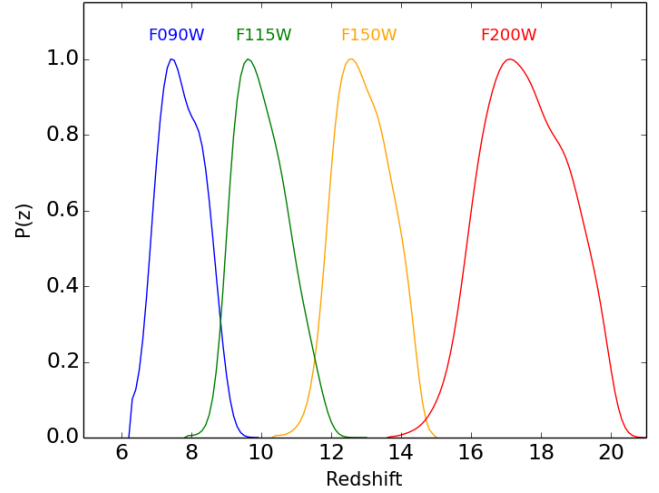


Figure 2. Redshift selection functions for our nominal $z \sim 8$, $z \sim 10$, $z \sim 13$, and $z \sim 17$ selections leveraging a Lyman-break selection identifying sources dropping out in the F090W, F115W, F150W, F200W, and F277W bands, respectively. The mean redshift of these selections is 7.7, 10.0, 12.9, and 17.6, respectively. These nominal redshift selections can be characterized as ranges with $z \sim 7 - 9$, $z \sim 9 - 11$, $z \sim 12 - 14$ and $z \sim 16 - 19$ (the approximate half-power points of the redshift selection functions)

the selection criteria. As we show below, when we discuss the redshift selection functions, these nominal redshift selections are better characterized as selections with $z \sim 7 - 9$, $z \sim 9 - 11$, $z \sim 12 - 14$ and $z \sim 16 - 19$ (the approximate half-power points of the redshift selection functions).

Given the significant variation in the composition of various $z \geq 8$ selections in the literature, we have purposefully required that sources show especially large Lyman breaks to maximize the robustness of the sources we select. The presence of a large spectral break is perhaps the most model-independent feature of star-forming galaxy at very high redshifts and will significantly less sensitive to uncertainties in the NIRCcam zeropoints than photometric redshift codes that rely on fits to the spectral energy distribution. As in Bouwens et al. (2015), sources are excluded from a Lyman break selection, if they meet the selection criteria of a higher-redshift sample.

Additionally, we require that sources show no significant flux blueward of the break. For this, we co-add the flux blueward of candidate Lyman breaks using the χ^2 statistic χ^2 defined in Bouwens et al. (2011, 2015) and which is equal to $\sum_i \text{SGN}(f_i)(f_i/\sigma_i)^2$ where f_i is the flux in band i in a consistent aperture, σ_i is the uncertainty in this flux, and $\text{SGN}(f_i)$ is equal to 1 if $f_i > 0$ and -1 if $f_i < 0$. Included in this statistic are the $B_{435}8475V_{606}I_{814}$, $B_{435}8475V_{606}I_{814}z_{090}Y_{105}$, $B_{435}8475V_{606}I_{814}z_{090}Y_{105}J_{115}J_{125}$, and $B_{435}8475V_{606}I_{814}z_{090}Y_{105}J_{115}J_{125}JH_{140}J_{150}H_{160}$ bands for our selections at $z \sim 8$, $z \sim 10$, $z \sim 13$, and $z \sim 17$, respectively. Sources are excluded from our selection if the χ^2 statistics in $0.2''$ -diameter, $0.35''$ -diameter, or scalable Kron apertures (using a Kron parameter of 1.2) exceeds 4, 6, 7, 8, and 9, when combining data from 1, 2, 3, 4, and 5 bands, respectively.

To ensure that sources in our selection corresponded to real objects, we require that sources be detected at 6σ in a stack of all bands redward of the break in a $0.35''$ -diameter aperture. We also require sources to be detected at 5σ in the band just redward of the break to ensure that the break is present at high significance. Sources are also required to be detected at 3.5σ in at least 5, 4, 4, and 3, independent

bands redward of the Lyman-break in our $z \sim 8$, $z \sim 10$, $z \sim 13$, and $z \sim 17$ selections.

Following our selection of candidate $z \sim 8$ -17 sources using the above criteria, redshift likelihood functions $P(z)$ were computed for each source using the EAZY photometric redshift code (Brammer et al. 2008). In fitting the photometry of individual sources, use of spectral templates from the EAZY_v1.0 set and Galaxy Evolutionary Synthesis Models (GALEV; Kotulla et al. 2009) was made. Nebular continuum and emission lines were added to the templates according to the prescription provided in Anders & Fritze-v. Alvensleben (2003), a $0.2Z_{\odot}$ metallicity, and scaled to a rest-frame EW for $H\alpha$ of 1300\AA . Sources are only retained in our $z > 6$ selections, if $>80\%$ of the integrated redshift likelihood is at $z > 5.5$, i.e., $P(z > 5.5) > 0.8$.

Finally, all candidate $z \geq 8$ galaxies are visually examined to exclude any sources associated with diffraction spikes, on the wings of early type galaxies, or in regions of the images with elevated background levels.

The approximate redshift distributions of these selections are illustrated in Figure 2 and derived using our selection volume simulations described in §4.1. Using these selection volume simulations, the mean redshifts inferred for our F090W, F115W, F150W, and F200W dropout selections are equal to 7.7, 10.0, 12.9, and 17.6, hence our nominal use of $z \sim 8$, $z \sim 10$, $z \sim 13$, and $z \sim 17$ to identify these samples throughout our paper.

3.2 $z \geq 8$ Selections

Applying our selection criteria to our fiducial reductions using GRIZLI, we identify 18 $z \sim 8$, 12 $z \sim 10$, 5 $z \sim 13$, and 1 $z \sim 17$ galaxies which satisfy all of our selection criteria. The apparent magnitude of these sources range from 25.8 to 28.4 mag. A list of these sources is presented in Table 2 and will be known as our primary selection. Figure 1 shows the colors of our selected $z \sim 8$ -17 sources relative to the two color criteria we utilize.

We also indicate in Table 2 which sources from our selections lie in earlier selections. Encouragingly, $\sim 67\%$ of the $z \geq 9$ candidates from our selection lie in previous $z \geq 9$ selections. This is a significantly higher level of overlap than was the case for the first set of $z \geq 9$ selections from the SMACS0723, CEERS, and Abell 2744 parallel data sets, thanks to the slightly more complete selections of $z \geq 8$ sources in Finkelstein et al. (2022b) and Donnan et al. (2022, v2) taking advantage of a much improved NIRC*am* zeropoint calibration.

We also pursue an alternate selection of $z \geq 8$ galaxies based on our NIRC*am* reductions using the PENCIL pipeline. We identify 22 $z \sim 8$, 13 $z \sim 10$, 3 $z \sim 13$, and 1 $z \sim 17$ galaxy candidates in that selection. Table A1 in Appendix A provides the coordinates, estimated redshifts, magnitudes, constraints on the Lyman break amplitudes, and estimated likelihood to lie at $z > 5.5$.

Comparing our two selections, we find $\sim 47\%$ of the sources in our primary selection are also present in our alternate selection, while $\sim 38\%$ of the sources in our alternate selection also occur in our primary selection. The percentage overlap between our selections is similar to the $\sim 50\%$ overlap frequently seen between different $z \sim 4$ -8 selections executed over the Hubble Ultra Deep Field with HST data (see §3.4 of Bouwens et al. 2015 for a discussion). The existence of differences between the two selections is not surprising given our use of two different reductions of the data to identify sources and measure fluxes.

In an effort to better understand why there is only modest overlap between the two selections, we compared the photometry of sources in catalogs where they are selected vs. where they are not selected. We found that most of the observed differences could be explained

by variations in the size of the spectral breaks for selected sources and the apparent flux blueward of the nominal spectral breaks.

3.3 $z \geq 8$ Selections from the Literature

Given the many challenges that exist in making use of the first *JWST* observations in identifying $z \geq 8$ galaxies, the uncertain NIRC*am* zeropoints being perhaps the largest (e.g. Adams et al. 2022), it is useful for us to provide an alternate assessment of the many $z \geq 9$ candidates which have been identified in the early *JWST* observations. This can help provide us with insight into both the reliability and completeness of earlier *JWST*/NIRC*am* selections.

There have been selections of $z \geq 8$ galaxies conducted by at least ten different teams, including Naidu et al. (2022a), Castellano et al. (2022), Adams et al. (2022), Atek et al. (2022), Yan et al. (2022), Donnan et al. (2022), Whitler et al. (2022), Labbé et al. (2022), Harikane et al. (2022a), and Finkelstein et al. (2022b). In general, these studies have focused on identifying sources from one or more of the same three data sets considered here, allowing for an extensive set of comparisons between the different selections and independent assessments of various $z \geq 8$ candidates.

3.3.1 Evaluation and Segregation into Different Subsamples

In this subsection, we focus on the $z \geq 8$ candidates identified over the three most studied *JWST* NIRC*am* fields (SMACS0723, CEERS, and Abell 2744 parallel), and provide an independent evaluation of their robustness. To provide this evaluation, we have performed $0.35''$ -diameter aperture photometry on all the identified candidates from Naidu et al. (2022a), Castellano et al. (2022), Adams et al. (2022), Atek et al. (2022), Yan et al. (2022), Donnan et al. (2022), Whitler et al. (2022), Finkelstein et al. (2022b), Labbé et al. (2022), and Harikane et al. (2022a). For papers where changes have occurred to the identified high-redshift sources, we consider the catalogs in each version of various papers. Not only is this useful for gaining perspective on progress that has been made, but we have found that some sources in earlier versions of papers also appear to be credible $z > 8$ candidates, and therefore we have included these sources in our analysis to be as comprehensive as possible. We perform photometry on both our fiducial and alternate reductions using GRIZLI and PENCIL, respectively.

We then look for the presence of a significant spectral break in sources and compute redshift likelihood distributions for candidates based on our derived photometry of the recent GRIZLI and PENCIL reductions. We then segregate sources into three different samples:

- (1) one where the cumulative probability of candidates lying at $z > 5.5$, i.e., $P(z > 5.5)$, exceeds 99% using the photometry we have performed on both NIRC*am* reductions utilized here,
- (2) one where $P(z > 5.5)$ is in excess of 80% and 50% for our fiducial and secondary reductions, in excess of 70% for both our fiducial and secondary reductions, or in excess of 50% and 80% for our fiducial and secondary reductions, but does not the former selection criteria, and
- (3) one which does not satisfy either of the former selection criteria.

We refer to (1) the first selection of sources from the literature as the “robust” sample, (2) the second selection as the “solid” sample, and (3) the third selection of sources as the “possible” sample.

Table 2. Selection of nominal $z \sim 8$, $z \sim 10$, $z \sim 13$, and $z \sim 17$ sources identified over three most studied imaging fields (SMACS0723, CEERS, and Abell 2744 parallel) in early *JWST* NIRCам observations from our GRIZLI sample.

ID	RA	DEC	z_{phot}	m_{UV} [mag]	Lyman Break ^a [mag]	$\Delta\chi^{2b}$	$p(z > 5.5)$	Lit ¹
$z \sim 8$ Selection								
GLASSP1Z-4049020480	00:14:04.908	-30:20:48.04	$6.7^{+0.0}_{-0.0}$	27.9 ± 0.2	>2.1	-5.8	0.938	
GLASSP2Z-4027418404	00:14:02.740	-30:18:40.44	$6.8^{+0.2}_{-0.1}$	27.8 ± 0.2	>2.4	-12.1	0.996	B22M
GLASSP1Z-4027520346	00:14:02.751	-30:20:34.66	$7.2^{+0.3}_{-0.4}$	28.4 ± 0.3	>2.2	-3.9	0.966	B22M
GLASSP1Z-4030120490	00:14:03.018	-30:20:49.03	$7.2^{+0.3}_{-0.4}$	28.2 ± 0.2	>2.2	-6.2	0.983	
GLASSP1Z-4047621148	00:14:04.769	-30:21:14.87	$7.2^{+0.3}_{-0.4}$	28.3 ± 0.3	>2.2	-7.7	0.993	
GLASSP1Z-4041221456	00:14:04.125	-30:21:45.65	$7.3^{+0.4}_{-0.5}$	28.4 ± 0.3	>2.0	-3.8	0.914	B22M
GLASSP1Z-3589121028	00:13:58.913	-30:21:02.82	$7.4^{+0.2}_{-0.3}$	28.0 ± 0.2	>2.6	-13.5	1.0	B22M
GLASSP1Z-3581321041	00:13:58.136	-30:21:04.19	$7.4^{+0.4}_{-0.4}$	28.4 ± 0.2	>2.0	-4.8	0.962	B22M
GLASSP1Z-4075621492	00:14:07.560	-30:21:49.20	$7.5^{+0.5}_{-0.5}$	28.3 ± 0.2	>2.0	-4.8	0.97	
GLASSP1Z-3577921174	00:13:57.792	-30:21:17.44	$7.6^{+0.4}_{-0.4}$	26.4 ± 0.1	2.3 ± 0.7	-56.3	1.0	B22M
S0723Z-3295626401	07:23:29.565	-73:26:40.17	$7.6^{+0.6}_{-0.6}$	27.7 ± 0.2	2.2 ± 1.7	-21.4	1.0	
GLASSP1Z-4049021453	00:14:04.905	-30:21:45.36	$7.6^{+0.5}_{-0.5}$	27.0 ± 0.2	>2.3	-2.2	0.861	
GLASSP1Z-3575621160	00:13:57.567	-30:21:16.02	$7.8^{+0.2}_{-0.4}$	28.5 ± 0.2	>1.9	-20.0	1.0	Le22
GLASSP1Z-4020821598	00:14:02.087	-30:21:59.85	$7.8^{+0.4}_{-0.5}$	27.2 ± 0.2	>2.7	-8.0	0.992	B22M
S0723Z-3201526042	07:23:20.159	-73:26:04.29	$7.8^{+0.3}_{-0.2}$	26.4 ± 0.1	>3.2	-41.1	1.0	D22,At22,Ad22,B22M
GLASSP2Z-4016419299	00:14:01.649	-30:19:29.90	$8.1^{+0.4}_{-0.4}$	27.8 ± 0.2	>2.3	-16.7	1.0	
S0723Z-3226926062	07:23:22.698	-73:26:06.24	$8.1^{+0.5}_{-0.2}$	25.8 ± 0.1	>3.6	-48.9	1.0	D22,At22,Ad22,B22M
GLASSP1Z-4009521308	00:14:00.950	-30:21:30.85	$8.3^{+0.3}_{-0.3}$	27.3 ± 0.1	>2.7	-5.0	0.937	
$z \sim 10$ Selection								
CEERSYJ-0012159472	14:20:01.212	52:59:47.29	$8.9^{+0.5}_{-0.5}$	27.6 ± 0.3	>1.7	-2.2	0.86	F22,B22M
CEERSYJ-9345150450	14:19:34.516	52:50:45.06	$9.2^{+0.8}_{-0.6}$	28.2 ± 0.3	1.5 ± 1.0	-10.5	0.997	
CEERSYJ-9586559217	14:19:58.654	52:59:21.77	$9.2^{+0.1}_{-0.2}$	27.1 ± 0.1	1.9 ± 0.7	-15.1	0.999	F22,W22
GLASSP1YJ-4003721456	00:14:00.378	-30:21:45.60	$9.2^{+0.8}_{-0.7}$	28.5 ± 0.2	>1.6	-4.1	0.953	B22M
CEERSYJ-9203050435	14:19:20.300	52:50:43.59	$9.8^{+0.8}_{-0.7}$	28.5 ± 0.3	>1.7	-8.9	0.989	
CEERSYJ-0012959481	14:20:01.290	52:59:48.12	$9.9^{+0.8}_{-0.8}$	27.8 ± 0.3	>1.8	-4.1	0.952	F22,B22M
CEERSYJ-9149352106	14:19:14.935	52:52:10.63	$10.0^{+0.7}_{-0.7}$	27.6 ± 0.2	1.8 ± 2.1	-4.7	0.956	
CEERSYJ-9353350378	14:19:35.337	52:50:37.87	$10.2^{+0.6}_{-0.7}$	27.9 ± 0.2	>1.7	-14.2	0.999	D22,F22,W22,B22M
GLASSP1YJ-4028622186	00:14:02.861	-30:22:18.69	$10.2^{+0.4}_{-0.4}$	26.7 ± 0.1	>3.1	-30.4	1.0	N22,C22,D22,H22,B22M
GLASSP1YJ-4002721259	00:14:00.278	-30:21:25.95	$10.6^{+0.6}_{-0.7}$	28.0 ± 0.2	>1.9	-5.6	0.975	D22
CEERSYJ-9026550577	14:19:02.654	52:50:57.74	$11.2^{+0.5}_{-0.5}$	27.8 ± 0.2	>1.6	-5.7	0.968	
GLASSP1YJ-4069421497	00:14:06.945	-30:21:49.73	$11.2^{+0.4}_{-0.4}$	26.8 ± 0.1	>1.9	-3.5	0.841	C22,B22M
$z \sim 13$ Selection								
CEERSH-9463556328	14:19:46.352	52:56:32.82	$11.6^{+0.4}_{-0.5}$	27.7 ± 0.2	1.5 ± 1.0	-9.9	0.995	D22,F22,H22,B22M
GLASSP2H-3597519291	00:13:59.756	-30:19:29.14	$12.1^{+0.2}_{-0.2}$	26.7 ± 0.1	1.8 ± 0.2	-21.6	1.0	N22,C22,D22,H22,B22M
S0723H-2522527555	07:22:52.258	-73:27:55.52	$12.9^{+0.9}_{-0.9}$	28.0 ± 0.2	2.2 ± 2.4	-4.8	0.961	At22,Y22
GLASSP2H-3576218534	00:13:57.627	-30:18:53.49	$13.7^{+1.0}_{-1.0}$	28.2 ± 0.2	>1.4	-10.2	0.996	
S0723H-2394130081	07:22:39.416	-73:30:08.17	$14.9^{+0.8}_{-0.7}$	26.9 ± 0.1	>1.7	-6.4	0.971	At22
$z \sim 17$ Selection								
CEERSK-9394956348	14:19:39.491	52:56:34.87	$16.3^{+0.3}_{-0.4}$	26.3 ± 0.1	1.7 ± 0.1	-8.7	0.987	D22,F22,H22,N22, Z22

¹ Ad22 = [Adams et al. \(2022\)](#), At22 = [Atek et al. \(2022\)](#), C22 = [Castellano et al. \(2022\)](#), D22 = [Donnan et al. \(2022\)](#), F22 = [Finkelstein et al. \(2022a,b\)](#), H22 = [Harikane et al. \(2022a\)](#), La22 = [Labbé et al. \(2022\)](#), N22 = [Naidu et al. \(2022a,b\)](#), W22 = [Whitler et al. \(2022\)](#), Y22 = [Yan et al. \(2022\)](#), B22 = This Work (primary selection), B22M = This Work (alternate selection), Z22 = [Zavala et al. \(2022\)](#)

^a Amplitude of Lyman break in mag

^b $\chi^2_{best,z>5.5} - \chi^2_{best,z<5.5}$

3.3.2 Results

We present these different samples in Table 3 and Tables B1–B5 of Appendix B. Interestingly enough, only 18 $z \sim 10$ and 3 $z \sim 13$ candidates from these fields satisfy our criteria for being robust. 75 of the reported candidates in the literature qualify as “solid” candidates, while 108 of these candidates qualify as “possible.”

Of the candidates we classify as “robust,” only 10 have an estimated redshift $z \geq 9$ using our fiducial photometry. The most consistent characteristics of sources in our robust lists is that they show either very pronounced (≥ 1.5 -mag) spectral breaks in the observed photometry or show two spectral breaks (Lyman + Balmer, as was a key aspect of the [Labbé et al. 2022](#) selection). Additionally, to the extent that the present compilation of “robust” $z \geq 9$ candidates

Table 3. Sample of $z \sim 10$, $z \sim 13$, and $z \sim 17$ candidate that we deem to be “robust” using our own photometry on two separate reductions of the NIRCcam Data.

ID	RA	DEC	z_{phot}^a	M_{UV}^*	Break [mag]	$\Delta\chi^{2b}$	$p(z > 5.5)^b$	Lit
Naidu et al. (2022a)								
GL-z11	00:14:02.857	-30:22:18.92	10.4/10.2 $^{+0.4}_{-0.4}$	-20.7	>3.1,>3.3	-30.4,-33.7	1.000,1.000	C22,D22,H22, B22,B22M
GL-z13	00:13:59.754	-30:19:29.10	12.4/12.1 $^{+0.2}_{-0.2}$	-21.0	1.8±0.2,2.1±0.2	-21.6,-20.0	1.000,1.000	C22,D22,H22, B22
Adams et al. (2022)								
3602	07:23:26.705	-73:26:10.56	9.0/9.5 $^{+1.2}_{-1.2}$	-19.5	>1.4,>2.0	-18.9,-20.4	1.000,1.000	D22
2779	07:22:35.053	-73:28:32.99	9.5/9.2 $^{+1.1}_{-1.3}$	-19.5	>2.5,>2.6	-6.6,-13.2	0.991,1.000	D22
Atek et al. (2022)								
SMACS_z10b	07:23:22.697	-73:26:06.23	8.9/8.1 $^{+0.3}_{-0.2}$	-20.8	>3.6,>3.9	-48.9,-49.8	1.000,1.000	D22
SMACS_z10c	07:23:20.158	-73:26:04.28	9.8/7.8 $^{+0.3}_{-0.2}$	-20.2	>3.2,3.4±2.5	-41.1,-40.3	1.000,1.000	D22
SMACS_z10a	07:23:26.240	-73:26:56.96	9.8/8.9 $^{+0.4}_{-0.5}$	-18.8	>2.8,>2.8	-25.5,-22.3	1.000,1.000	D22
Donnan et al. (2022, v2)								
43031	07:23:27.846	-73:26:19.78	8.6/7.9 $^{+0.5}_{-0.5}$	-18.4	>2.5,>3.0	-20.7,-22.2	1.000,1.000	W22,F22,B22,B22M H22,B22,B22M, F22
22480	07:22:45.808	-73:27:46.57	9.7/8.7 $^{+1.3}_{-1.3}$	-18.5	>1.4,>1.8	-10.0,-11.2	0.997,0.998	
30585	14:19:35.334	52:50:37.90	10.6/10.2 $^{+0.6}_{-0.7}$	-19.4	>1.7,2.0±2.5	-14.2,-9.5	0.999,0.990	
32395_2	14:19:46.353	52:56:32.81	12.3/11.6 $^{+0.4}_{-0.5}$	-19.9	1.5±1.0,1.5±1.2	-9.9,-9.1	0.995,0.993	
Donnan et al. (2022, v1)†								
38681	07:23:28.099	-73:26:20.10	8.6/8.0 $^{+0.6}_{-0.7}$	-19.4	>1.8,>1.7	-7.8,-9.7	0.993,0.996	
Labbé et al. (2022)								
35300	14:19:19.358	52:53:16.01	9.3/9.4 $^{+1.0}_{-1.0}$	-19.0	>1.4,1.7±1.5	-7.8,-17.2	0.993,1.000	F22,B22M
14924	14:19:30.272	52:52:51.01	9.9/8.8 $^{+0.2}_{-0.2}$	-20.1	1.1±0.5,0.9±0.5	-25.1,-22.4	1.000,1.000	F22
16624	14:19:22.741	52:53:31.60	10.0/8.6 $^{+0.3}_{-0.2}$	-20.9	1.0±0.2,1.2±0.2	-17.7,-18.4	1.000,1.000	F22
21834	14:19:36.533	52:56:21.76	10.8/9.3 $^{+1.1}_{-0.9}$	-19.0	1.0±1.5,0.7±1.3	-11.4,-10.7	0.998,0.998	F22
Harikane et al. (2022a, v1)†								
GL-z9-6	00:13:57.110	-30:19:31.53	8.7/8.1 $^{+0.5}_{-0.6}$	-18.8	>1.7,>1.9	-9.2,-12.8	0.993,0.999	Le22
GL-z9-12	00:14:01.896	-30:18:56.89	10.2/10.1 $^{+0.6}_{-0.5}$	-18.7	>1.7,>1.9	-14.6,-23.1	1.000,1.000	
Whitler et al. (2022)								
EGS-39117	14:20:02.808	52:59:17.91	9.0/8.8 $^{+0.1}_{-0.2}$	-20.5	1.2±0.1,1.5±0.2	-23.1,-20.9	1.000,1.000	F22
This Work (Primary Selection)								
GLASSP2H-3576218534	00:13:57.629	-30:18:53.43	13.7/13.7 $^{+1.0}_{-1.0}$	-19.6	>1.4,>1.8	-10.2,-11.3	0.996,0.999	B22M
This Work (Secondary Selection)								
GLASSP2Z-3553419246	00:13:55.345	-30:19:24.63	8.6/8.3 $^{+0.3}_{-0.3}$	-19.8	2.1±1.1,>3.0	-15.9,-22.1	1.000,1.000	

¹ Ad22 = Adams et al. (2022), At22 = Atek et al. (2022), C22 = Castellano et al. (2022), D22 = Donnan et al. (2022), F22 = Finkelstein et al. (2022a,b), H22 = Harikane et al. (2022a), La22 = Labbé et al. (2022), N22 = Naidu et al. (2022a,b), W22 = Whitler et al. (2022), Y22 = Yan et al. (2022), B22 = This Work (fiducial selection), B22M = This Work (alternate selection), Z22 = Zavala et al. (2022)

^a Presented are the photometric redshift as reported in the earlier work and as estimated here based on the GRIZLI reductions

^b The different measurements provided are based on the two different reductions of the NIRCcam data utilized in this analysis.

† While these candidates were identified in earlier versions of these manuscripts, they did not make it into the final versions of these manuscripts. Nonetheless, our analysis suggests they are “robust” $z > 5.5$ sources.

* For simplicity, no account is made for lensing magnification for sources over the MACS0723 and Abell 2744 parallel fields.

overlap with the redshift ranges and fields examined by Harikane et al. (2022a), three of the four sources from our compilation, i.e., GL-z11, GL-z13, and 32395_2 (Donnan et al. 2022; Finkelstein et al. 2022a), receive robust designations in Harikane et al. (2022a), with $\Delta\chi(z_{low})^2 - \chi(z_{high})^2$ equal to 71.9, 72.3, and 14.5, respectively, each of which is well above their $\Delta\chi^2 > 9$ selection criterion

for secure sources. This is reassuring and gives us confidence that at least for this subset of $z \geq 9$ candidates, the inferred redshifts might be reasonably secure.

From these numbers, it is clear that the majority of $z \geq 9$ candidates identified to date only qualify as “possible” $z \geq 9$ candidates and do not meet the higher quality standards required to be classified as “robust” or “solid.” Interestingly enough, essentially all $z \geq 8$ studies

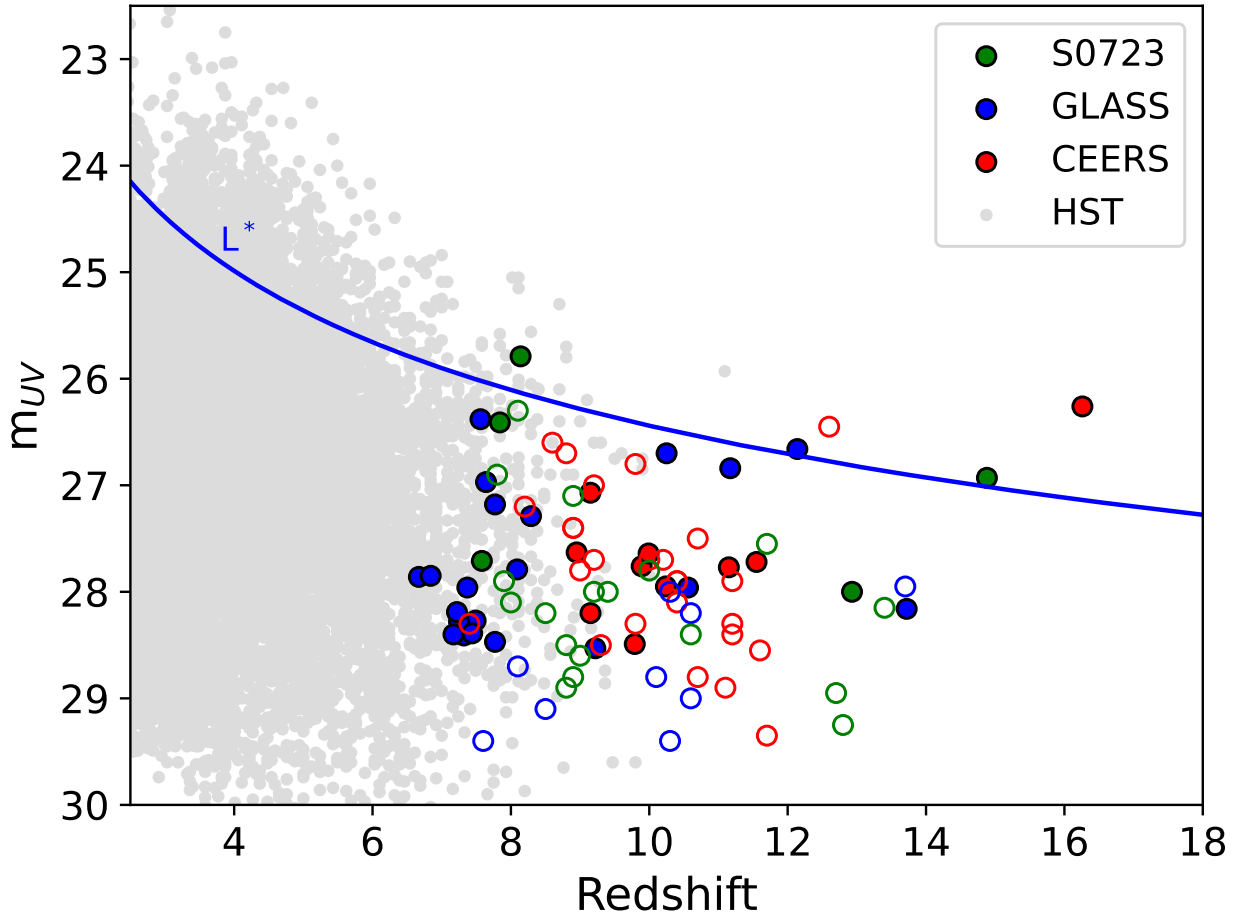


Figure 3. Apparent magnitude and estimated redshifts of $z \geq 7$ candidate galaxies identified over the *JWST*/NIRCam SMACS0723 (solid green circles), GLASS parallel (solid blue circles), and CEERS fields (solid red circles) from our searches of the GRIZLI data sets. The open symbols indicate other $z \geq 8$ galaxy candidates that have been identified in the literature and qualify as “robust” or “solid” $z \geq 8$ candidates according to our own SED fits and photometry. For context, we show the magnitudes and redshifts of sources that have derived from a comprehensive set of blank and lensing fields observed with HST (Bouwens et al. 2021, 2022a). The blue solid line shows the apparent magnitude of sources with an absolute magnitude of -21 , which is an approximate characteristic luminosity of galaxies at $z \geq 3$ (Steidel et al. 1999; Reddy & Steidel 2009; Bouwens et al. 2015, 2021; Finkelstein et al. 2015; Bowler et al. 2015).

presenting significant samples of $z \geq 8$ candidates from the first *JWST* fields, e.g., Atek et al. (2022), Donnan et al. (2022), Harikane et al. (2022a), Yan et al. (2022), all contain sources that lie in the “possible” category given our photometry. Interestingly enough, of the candidates we grade as “robust,” “solid,” and “possible” and where we compute photometric redshifts $z \geq 9$, 90%, 26%, and 5% are also independently reported as a $z \geq 8$ candidate galaxy in a separate manuscript from the literature.

Figure 3 shows the distribution of the sources we find from our GRIZLI reductions over the three NIRCam fields (SMACS0723, GLASS parallel, and CEERS) in redshift and *UV* luminosity vs. the comprehensive earlier selection of $z \sim 2$ –11 sources from Hubble constructed by Bouwens et al. (2021, 2022a). We also show the “robust” or “solid” $z \geq 8$ galaxy candidates from the earlier studies with *JWST*.

In Figure 4, we show the number of sources that are contained in our literature subsamples of “robust,” “solid,” and “possible” candidates as a function of redshift. The number of “solid” and “possible” candidates at $z > 11.5$ are $8\times$ and $24\times$ larger than those which we grade as “robust.” Clearly, it is essential that higher quality *JWST* data become available for sources in these samples to determine the fraction that are actually at $z > 11.5$.

3.3.3 Characterization of Literature Subsamples

To help interpret the quality of the $z \geq 8$ candidates that we segregated into different categories, we derive median fluxes for candidates in each category. Prior to the median stacking, a renormalization of the fluxes in individual sources is performed such that the F200W, F277W, and F356W band fluxes for the $z \sim 10$, $z \sim 13$, and $z \sim 17$ samples, respectively, are 36 nJy. The results are presented in Table C1 of Appendix C.

The most significant difference between the different stacks is the flux blueward of the break. For both the “robust” and “solid” stacks, no significant flux is present blueward of the putative Lyman breaks and large Lyman breaks are seen, i.e., ≥ 1.8 mag. However, for the “possible” stack, not only is the flux in the median stacks nominally significant 1 – 2σ in individual bands, but the putative breaks are smaller, i.e., ~ 1.0 – 1.5 mag. Because of such characteristics, the reliability of sources in the “possible” samples is lower, as indicated also by the much greater likelihood these sources show for being at lower redshifts from the individual SED fit results.

To provide some measure of the quality and completeness of earlier selections of $z \geq 8.5$ galaxies derived from the first *JWST* fields, we have calculated the total number of “robust”+“solid” $z \geq 8.5$ candidates that have been identified to ~ 29 mag over various *JWST* fields

Table 4. Assessment of the purity and completeness of various $z \sim 10$, $z \sim 13$, and $z \sim 17$ selections on the basis of independent selections made over the same fields and leveraging our own independent photometry.[†]

Sample	# of Sources ^a	Purity (Robust) ^b	Purity (Robust+Solid) ^c	Completeness ^d	Fraction of Total Candidates ^e
This Work (Fiducial)	16	0.250	0.875	0.203	0.105
This Work (Alternate)	21	0.238	0.762	0.232	0.137
Adams et al. (2022)	4	0.500	1.000	0.129	0.043
Atek et al. (2022, v2)	10	0.300	0.500 [‡]	0.161	0.108
Atek et al. (2022, v1)	15	0.200	0.333 [‡]	0.161	0.162
Castellano et al. (2022, v2)	6	0.333	0.667	0.333	0.286
Castellano et al. (2022, v1)	7	0.286	0.571	0.333	0.333
Donnan et al. (2022, v2)	31	0.258	0.903	0.364	0.176
Donnan et al. (2022, v1)	34	0.176	0.588	0.260	0.193
Finkelstein et al. (2022b)	23	0.261	0.869	0.588	0.371
Harikane et al. (2022a, v2)	13	0.231	0.461	0.200	0.155
Harikane et al. (2022a, v1)	13	0.385	0.538	0.233	0.155
Labbé et al. (2022)	5	0.800	1.000	0.147 [*]	0.081 [*]
Naidu et al. (2022a)	2	1.000	1.000	0.333	0.333
Whitler et al. (2022, v2)	6	0.167	0.667	0.118	0.097
Whitler et al. (2022, v1)	8	0.125	0.750	0.176	0.129
Yan et al. (2022)	64	0.000	0.234 [‡]	0.484	0.608

[†] We emphasize that the results we present are completely reliant on the photometry we derive for the candidates from our two reductions and the SED template sets we have available for our redshift likelihood calculations. As such, these results are merely indicative, and clearly the ultimate arbiter of the purity and completeness of individual selections will be deep spectroscopy with *JWST*.

^a Number of $z \geq 8.5$ candidates identified in the magnitude range well probed in most studies in the literature (i.e., < 29 mag)

^b Fraction of $z \geq 8.5$ candidates from this study that satisfy our criteria for being “robust” $z \geq 8.5$ candidates.

^c Fraction of $z \geq 8.5$ candidates from this study that satisfy our criteria for being “robust” or “solid” $z \geq 8.5$ candidates.

^d Fraction of the total set of “robust” and “solid” $z \geq 8.5$ candidates (Tables 3, B1, and B2) identified in a given study. Only the search fields utilized in a study are considered for these completeness estimates.

^e Fraction of the total number of $z \geq 8.5$ candidates identified in a given study. Only the search fields utilized in a study are considered for these completeness estimates.

^{*} We would not expect the Labbé et al. (2022) selection to be an especially complete representation of star-forming galaxies at $z > 6$, given their choice to select only those galaxies with prominent Balmer breaks.

[‡] The purity of selections focusing on the SMACS0723 cluster and parallel field are likely lower than the other selections due to the lack of especially sensitive F115W data over the fields.

by our selection or those in the literature and quantified the fraction of these candidates that have been identified in various studies. We present this fraction as the completeness of each selection in Table 4. In estimating the completeness, we only consider the fields included in a given selection. As one example, since Harikane et al. (2022a) do not search for $z \sim 8$ –11 F090W-dropout galaxies as part of their $z \sim 9$ selection, we do not treat compelling $z \sim 8$ –11 galaxies found over other fields as contributing to our assessment of completeness in their study.

3.3.4 Evaluation of Earlier $z \geq 8$ Selections

In Table 4, we also present an approximate “purity” for each selection by dividing the number of “robust” candidates in each selection by the total number of reported candidates in a study as well as the number of “robust” and “solid” candidates in a given study. In grading individual candidates from various studies, we only include sources which *UV* magnitudes brightward of 29 mag to limit our analysis to those sources with the highest S/N and to increase the probability that sources will be selected as part of multiple studies.

We caution that the results we obtain here are completely reliant on the photometry we derive for the candidates from our two reductions and the SED template sets we utilize in our analysis. As such, these results (and the remarks in the paragraphs which follow) should be taken as merely indicative, and *clearly the ultimate arbiter* of the

purity and completeness of individual selections will be deep spectroscopy with *JWST* (e.g. Roberts-Borsani et al. 2022; Curtis-Lake et al. 2022). For the purposes of this calculation, we treat sources with a “possible” designation as corresponding to lower-redshift interlopers, but clearly there is some uncertainty in this designation and many candidates we grade in this category might well prove to be at $z \geq 8$.

There are a few noteworthy results to notice in the results presented in this table. First of all, there has been a clear improvement in both the purity and completeness of most $z \geq 8$ samples since NIRC*am* data from *JWST* became public, as one might expect to improvements in the NIRC*am* zeropoint calibrations. As one example, the purity of the Donnan et al. (2022) selections – in terms of sources graded either “robust” or “solid” – have improved from 59% (v1) to 90% (v2). Other newer analyses which are able to take advantage of the improved zeropoint calibrations are the fiducial and secondary selections from the present analysis as well as those from Finkelstein et al. (2022b); these selections feature a purity of 88%, 76%, and 87%, respectively. Achieving a high purity appears to have been more difficult for analyses that focus on the SMACS0723 data set (e.g., Atek et al. 2022; Yan et al. 2022 but see however Adams et al. 2022), likely due to the significantly shallower F115W observations available in the first *JWST* data over that field.

Second, selections that focus on the most luminous galaxies at $z \geq 8$, i.e., Naidu et al. (2022a,b); Adams et al. (2022), or selections

Table 5. Fraction of sources in common between various $z \geq 8$ selections relative to the total possible

	H22	D22	B22	B22M	F22	C22	At22	La22	W22	Y22
H22	13/13	—	—	—	—	—	—	—	—	—
D22	5/16 (3/16) ^{b,c}	31/31	—	—	—	—	—	—	—	—
B22	6/15 (5/16)	7/43 (5/50)	21/21	—	—	—	—	—	—	—
B22M	4/14 ^b	5/40 (4/46)	10/27	16/16	—	—	—	—	—	—
F22	2/6 (2/5)	9/30 (8/35)	7/27 (7/28)	6/28 (6/29)	23/23	—	—	—	—	—
C22	3/11 ^b	2/7 ^b (2/6) ^b	3/10 ^b (2/11) ^b	1/12 ^b	— ^a	6/6	—	—	—	—
At22	0/4	3/18 (1/29)	2/10 (2/15)	0/10 (0/15)	— ^a	— ^a	10/10	—	—	—
La22	— ^a	0/22 (0/25)	1/16	1/16	4/23 (4/24)	— ^a	— ^a	5/5	—	—
W22	— ^a	1/22 (2/26)	3/15 (2/18)	2/16 (2/18)	3/25 (3/28)	— ^a	— ^a	0/11	6/6	—
Y22	0/46	0/75 (0/80)	1/65 (1/66)	0/64 (0/65)	— ^a	— ^a	1/73 (2/78)	— ^a	— ^a	64/64

^aThere is no overlap between specific fields and redshift ranges utilized in the two selections being compared.

^bRemarkably, approximately half of the overlap between these studies are the two bright sources from [Naidu et al. \(2022a\)](#) and [Castellano et al. \(2022\)](#). If we exclude those two sources from consideration, overlap between the selections is only $\sim 10\%$.

^cFraction in parentheses indicates the overlap in the initial versions of the catalogs from these papers. In the majority of cases, the fraction in the updated versions is higher.

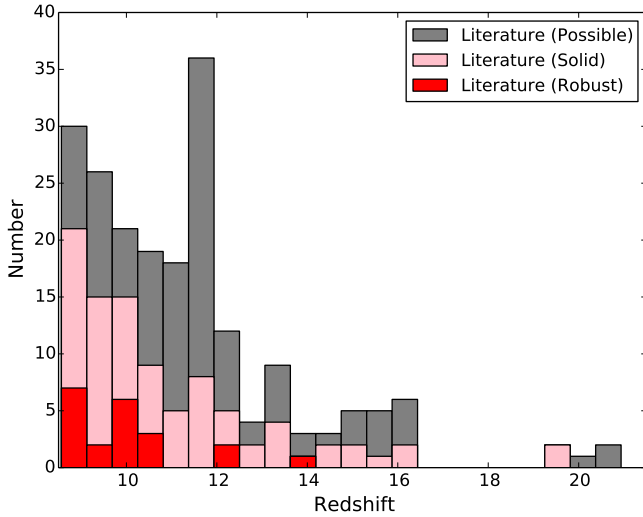


Figure 4. Number of sources in our literature samples of "robust," "solid," and "possible" sources vs. redshift (*red*, *pink*, and *gray* shaded histograms, respectively). The redshift of any given source is taken to be equal to the redshift of the study where it is presented in the literature for our "solid" and "possible" samples and the geometric mean redshift for sources in our "robust" sample. There are $8\times$ more "solid" and $24\times$ more "possible" sources reported in the literature at $z > 11.5$ than there are "robust" sources, illustrating the potentially large uncertainties in the overall number of bona-fide star-forming galaxies at very high redshifts. Given the uncertainties, it is clearly imperative to definitively quantify the redshifts of many of these candidates to determine how rapidly galaxies assemble in the early universe.

which focus on sources with multiple spectral breaks (e.g. [Labbé et al. 2022](#)) show a much higher reliability than those that focus on a broader selection of sources. Based on the present analyses, we find 100% purity for all three of these selections in our analysis. This contrasts with more ambitious selections aiming to select the bulk of the star-forming galaxies at $z \geq 8$, e.g., [Donnan et al. \(2022\)](#), [Harikane et al. \(2022a\)](#), [Finkelstein et al. \(2022b\)](#), and the present selections where $\sim 25\%$ of the sources in these selections are graded as "robust," 50-60% of the sources are graded as "solid," and the final $\sim 15\%$ of the sources in such selections are graded as "possible."

A third striking result is the large differences in the completeness of selections. The majority of the analyses only include a fraction ($\lesssim 35\%$) of the candidates we grade as "solid" or "robust" in our analysis. In many analyses, this appears to have been the result of a clear choice to include only those sources which appear to be the most reliable, either because higher amplitude Lyman breaks are required (*this work*) or because the SED fits to $z > 8$ solutions are required to give a much lower χ^2 ($\Delta\chi^2 > 9$) than lower redshift fits ([Harikane et al. 2022a](#)). Nevertheless, the [Finkelstein et al. \(2022b\)](#) selection appears to perform the best as far as completeness is concerned, showing a $\sim 2\times$ higher completeness in their identification of "solid"+"robust" $z \geq 8$ sources than most of the other analyses and also successfully selecting the $z \geq 8$ sources found by [Labbé et al. \(2022\)](#) with prominent Balmer breaks (Table 3). The latter sources mostly miss our own selections due to their Lyman breaks having a smaller amplitude than ≥ 1.5 mag required to be included in our own samples.

One consequence of the relatively low estimated completeness for most selections is only a modest (~ 20 - 35%) overlap between $z \geq 8$ selections. Table 5 quantifies the number of sources that are in common for differing selections over the same fields out of some total possible. Nevertheless, it is worthwhile noting that there has been an improvement in the overlap between samples. Initially, most

of the overlap between studies was confined to a few bright $z \sim 10$ –12 sources such as have been found by Naidu et al. (2022a) and Castellano et al. (2022) and perhaps 10–15% of the rest, but now the overlap is approximately $\sim 30\%$ between selections, approaching the $\sim 50\%$ overlap seen in $z \sim 4$ –8 selections obtained by HST over the Hubble Ultra Deep Field (Beckwith et al. 2006), e.g., see §3.4 of Bouwens et al. (2015) where overlap with other $z \sim 7$ –8 selections (e.g. McLure et al. 2013; Schenker et al. 2013) is discussed.

4 LUMINOSITY FUNCTION RESULTS

In this section, we make use of the rather small samples of high-likelihood $z \geq 8$ galaxy candidates over the three most well studied *JWST* fields to derive *UV* LF results. We begin with direct determinations of the LF results using our own selections and then move onto determinations based on collective samples of $z \geq 8$ galaxies identified in the present and previous studies. We conclude this section with a comparison of these results with several previous determinations.

4.1 Results Using Our Own Samples

We begin by describing LF results derived using our own $z \geq 8$ samples constructed from our fiducial reductions of the available *JWST* data.

Given the small number of sources in each of our samples, we derive LF results using the $1/V_{\max}$ technique and assuming Poissonian statistics. As in our own earlier analyses, we derive LF results by maximizing the likelihood \mathcal{L} of producing the observed distribution of apparent magnitudes given some model LF:

$$\mathcal{L} = \prod_{field} \Pi_i p(m_i) \quad (1)$$

where we take the likelihood of LF results derived over the set of fields we select sources and over a set of apparent magnitude intervals m_i .

Given the lack of F090W observations over the CEERS fields and the limited depth of F115W observations over SMACS0723, we only consider sources in the GLASS parallel field for our $z \sim 8$ LF determination and sources over the GLASS parallel and CEERS fields for our $z \sim 10$ LF determinations. For our $z \sim 13$ and $z \sim 17$ determinations, we consider sources over the GLASS parallel, SMACS0723, and CEERS fields. For simplicity and because none of our $z \geq 12$ candidates lie within $<60''$ to the high magnification areas of the Abell 2744 and SMACS0723 clusters, we ignore the impact of lensing magnification on our LF results.

Since we are assuming Poissonian statistics, the probability of finding $n_{observed,i}$ sources

$$p(m_i) = e^{-n_{expected,i}} \frac{(n_{expected,i})^{n_{observed,i}}}{(n_{observed,i})!} \quad (2)$$

where $n_{observed,i}$ is the number of observed sources in magnitude interval i while $n_{expected,i}$ is the expected number given some model LF. We compute the number of expected sources $n_{expected,i}$ based on some model LF ϕ_j using the equation

$$n_{expected,i} = \sum_j \phi_j V_{i,j} \quad (3)$$

where $V_{i,j}$ is the effective volume over which a source in the magnitude interval j might be both selected and have a measured magnitude in the interval i .

We compute the selection volume for our samples by inserting artificial sources with various redshift and apparent magnitudes at random positions within the NIRCам images for each of these fields

Table 6. Binned LF Results for Galaxies at $z \geq 8$

M_{UV}	$\phi^* [\text{mag}^{-1} \text{Mpc}^{-3}]$
$z \sim 8$ galaxies	
−21.13	0.000046±0.000036
−20.13	0.000044±0.000036
−19.13	0.001050±0.000414
$z \sim 10$ galaxies	
−20.49	0.000018±0.000016
−19.49	0.000130±0.000068
$z \sim 13$ galaxies	
−20.96	0.000010±0.000008
−19.96	0.000032±0.000032
$z \sim 17$ galaxies	
−21.96	0.000018±0.000014

Table 7. Best-fit parameters derived for Schechter and double power-law fits to the present $z \geq 8$ *UV* LF results

Redshift	$\phi^* [10^{-5} \text{mag}^{-1} \text{Mpc}^{-3}]$	$M^* [\text{mag}]$	α	β
Schechter				
8	5.7 ^{+5.2} _{−2.7}	−21.15 (fixed)	−2.58±0.39	—
10	2.6 ^{+1.0} _{−0.7}	−21.15 (fixed)	−2.38 (fixed)	—
13	1.3 ^{+0.9} _{−0.6}	−21.15 (fixed)	−2.71 (fixed)	—
17	1.0 ^{+2.3} _{−0.8}	−21.15 (fixed)	−3.15 (fixed)	—
Double Power-Law				
8	102 ⁺³⁰ _{−24}	−19.67 (fixed)	−2.17 (fixed)	−3.75 (fixed)
10	28 ⁺¹¹ _{−8}	−19.67 (fixed)	−2.35 (fixed)	−3.75 (fixed)
13	22 ⁺¹⁵ _{−9}	−19.67 (fixed)	−2.62 (fixed)	−3.75 (fixed)
17	26 ⁺⁵⁹ _{−21}	−19.67 (fixed)	−2.98 (fixed)	−3.75 (fixed)

Table 8. Binned LF Results derived based on Sources in all Public Analyses^a

M_{UV}	$\phi^* [\text{mag}^{-1} \text{Mpc}^{-3}]$
$z \sim 10$ Robust/Solid	
−20.5	[0.000012, 0.000064]
−19.5	[0.000012, 0.000148]
−18.5	[0.000024, 0.000412]
$z \sim 13$ Robust/Solid	
−20.5	[0.000001, 0.000041]
−19.5	[0.000006, 0.000260]
−18.5	[0.000000, 0.000559]
$z \sim 17$ Robust/Solid	
−21.5	[0.000000, 0.000007]
−20.5	[0.000000, 0.000029]
−19.5	[0.000000, 0.000155]

^a Upper and lower bounds correspond to the inferred volume densities of our “solid” and “robust” literature selections, respectively, derived by dividing the number of sources in each of those selections by the available volume for *detecting* sources down to a given *UV* luminosity.

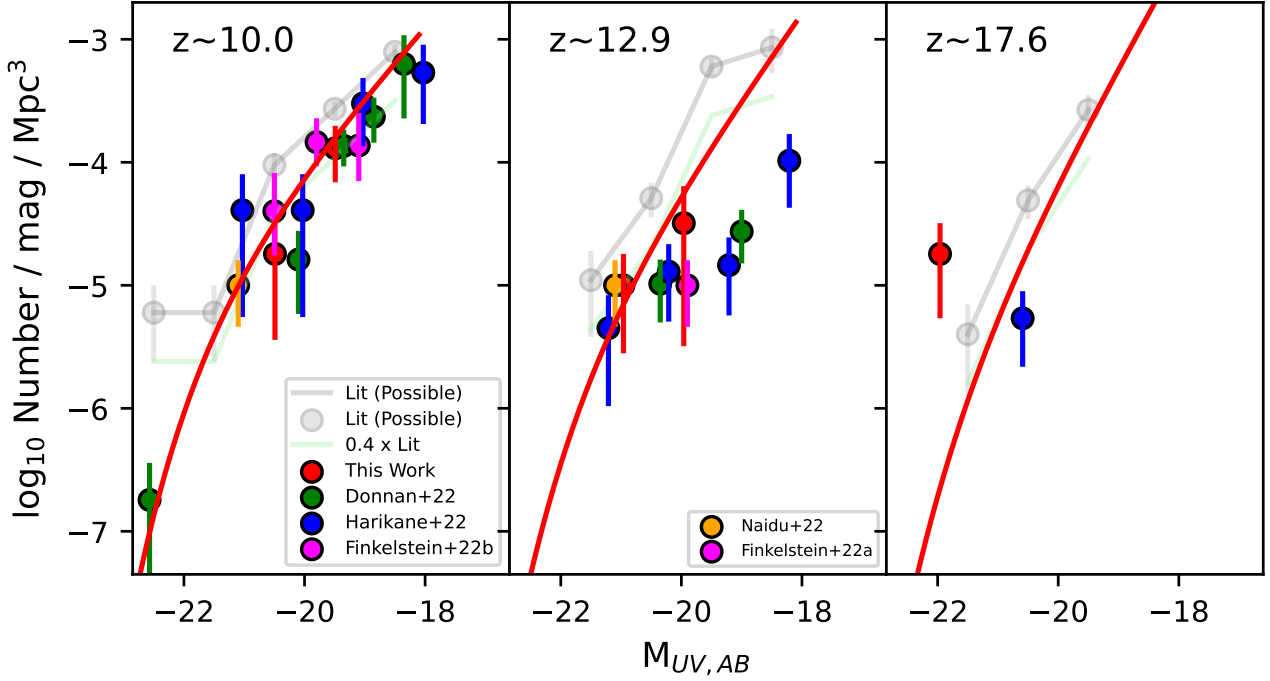


Figure 5. Determinations of the *UV* LF including all of the $z \geq 8$ candidates from the literature (shaded grey points) compared against other determinations of the $z \sim 10$ (left), $z \sim 13$ (center), and $z \sim 17$ (right) *UV* LF using new *JWST*/NIRCam data. Schechter and stepwise *UV* LFs derived using our own fiducial samples are shown with the red lines and circles, respectively, while those from [Naidu et al. \(2022a\)](#), [Donnan et al. \(2022\)](#), [Finkelstein et al. \(2022a,b\)](#), and [Harikane et al. \(2022a\)](#) are shown with the gold, green, magenta, and blue points, respectively. Gray lines are drawn connecting the gray points (to help delineate the LF derived from the full literature sample of sources). The reason the gray line has a much higher normalization than any LF in the literature is due to there being a much larger number of $z \geq 9$ candidates reported thus far over the SMACS0723, GLASS parallel, and CEERS fields than are present in any one individual analysis. A better match with the early *UV* LF results from *JWST* can be obtained by multiplying the shaded gray region by 0.4 (shown with the green line). These results suggest that either early *JWST* LF results in individual analyses are too low (due to incompleteness) or that early selections suffer from substantial ($\geq 50\%$) contamination from lower-redshift galaxies.

and then attempting both to detect the sources and select them using our $z \sim 8$, $z \sim 10$, $z \sim 13$, and $z \sim 17$ selection criteria. We assume the *UV*-continuum slopes of sources to have a mean value of -2.3 , with a 1σ scatter of 0.4 . These *UV*-continuum slopes are in reasonable agreement with determinations available on the basis of both HST+Spitzer data (e.g., [Dunlop et al. 2013](#); [Wilkins et al. 2016](#); [Stefanon et al. 2022b](#)) and now *JWST* data ([Topping et al. 2022](#); [Cullen et al. 2022](#)).

Additionally, we adopt point-source sizes for the artificial sources we inject into various images in our simulation and recovery experiments. While the present size assumptions are not especially different from that found for galaxies at $z \sim 8$ – 17 , both using earlier HST observations and now using *JWST* observations ([Naidu et al. 2022a,b](#); [Ono et al. 2022](#)), they may lead to a slight overestimate of the total selection volume. While it is worthwhile keeping this in mind for the discussion which follow, these uncertainties are likely small in comparison to the very large uncertainties in the total number of bona-fide $z \geq 8$ galaxies over these fields (amongst the many sources from the literature we have graded as “possible”).

We derive both determination of the *UV* LF results in 0.5-mag bins and determinations of the best-fit Schechter function and double power-law fits using the following functional form:

$$\phi(M) = \frac{\phi^*}{10^{0.4(M-M^*)(\alpha+1)} + 10^{0.4(M-M^*)(\beta+1)}} \quad (4)$$

where ϕ^* is normalization, α is the faint-end slope, β is the bright-

end slope, and M^* indicates some characteristic luminosity where there is a transition between the two regimes.

For the Schechter function results, we fix the M^* to -21.15 mag consistent with the $z \geq 7$ *UV* LF derived by [Bouwens et al. \(2021\)](#), while we fix α to -2.38 , -2.71 , and -3.15 at $z \sim 10$, $z \sim 13$, and $z \sim 17$ consistent with an extrapolation of the LF fit results of [Bouwens et al. \(2021\)](#) to the respective redshifts. For our double power-law fit results, we fix M^* to -19.67 and $\beta = -3.75$ to match the *UV* LF fit results of [Bowler et al. \(2020\)](#) at $z \sim 9$. We fix $\alpha = -2.17$, -2.35 , -2.62 , -2.98 at $z \sim 8$, $z \sim 10$, $z \sim 13$, and $z \sim 17$ consistent with the fitting formula [Bowler et al. \(2020\)](#) provide for evolution of the *UV* LF using a double power-law parameterization.

We present our binned *UV* LF results at $z \sim 10$, $z \sim 13$, and $z \sim 17$ LF results in both Table 6 and Figure 5. The parameterized fit results are presented in Table 7 and on Figure 5 as red lines. We also derived *UV* LF results at $z \sim 8$ as a test of our procedures for deriving *UV* LFs at $z \geq 10$. The results are shown in both Figure D1 from Appendix D and Tables 6–7. Encouragingly the results we obtain are consistent with the earlier determinations we obtained from HST data in [Bouwens et al. \(2021\)](#).

The present *UV* LF results appear to be fairly similar to the *UV* LF results of [Donnan et al. \(2022\)](#) and [Harikane et al. \(2022a\)](#) at $z \sim 9$ – 11 . At $z \sim 13$, we find a ~ 1.5 – $2\times$ higher volume density of sources than [Donnan et al. \(2022\)](#), [Harikane et al. \(2022a\)](#), and [Finkelstein et al. \(2022a\)](#), and at $z \sim 17$, the volume density we find for sources is $\sim 3\times$ higher than what [Harikane et al. \(2022a\)](#) recover. At the bright end of the $z \sim 10$ – 13 LFs, our results are very similar

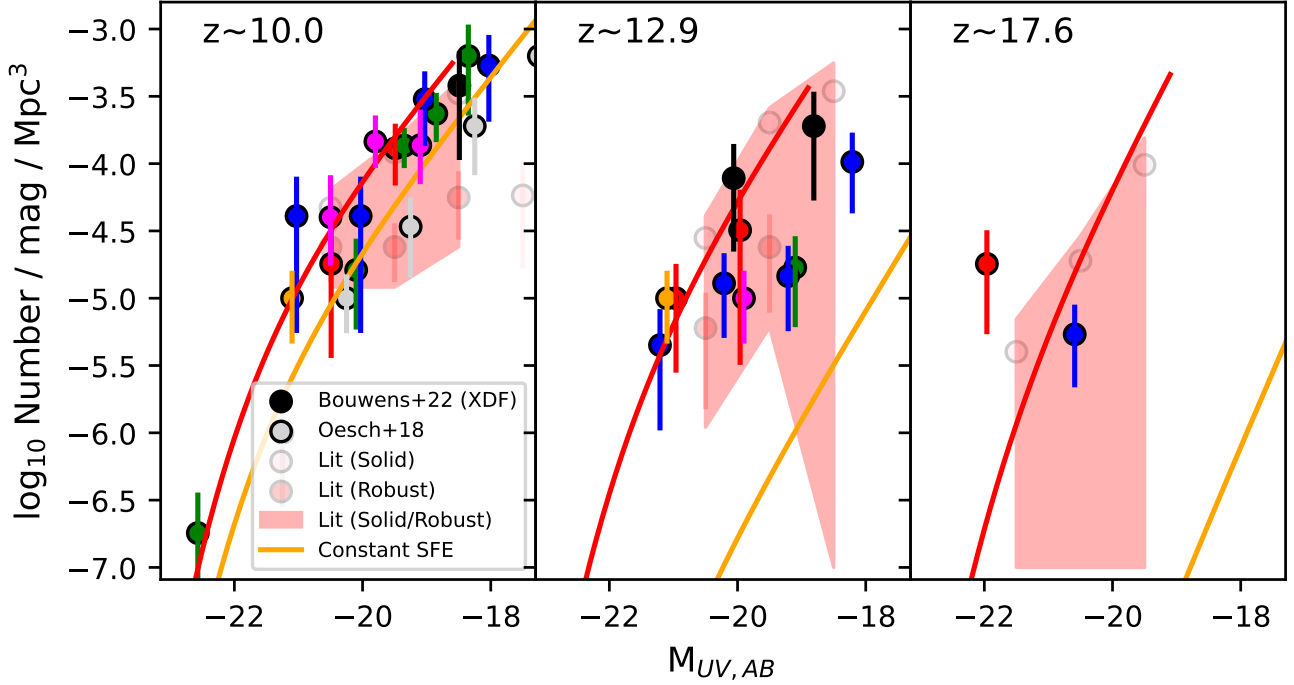


Figure 6. Illustration of how much higher new determinations of the UV LFs are with $JWST$ than the expected results assuming constant star formation rate efficiency (yellow line: Mason et al. 2015). The presented LF constraints are similar to those shown on Figure 5 but also include the results from Bouwens et al. (2022b) (black solid circles) over the HUDF/XDF (Beckwith et al. 2006; Illingworth et al. 2013) and Oesch et al. (2018) derived from HST observations alone (gray solid circles). The partially transparent pink and red points indicate the LF results derived alone from the “solid” and “robust” candidates, respectively. The shaded red region gives UV LF results one would obtain including all the literature candidates in our “robust” list, but no more than in our “solid” list of candidates. Given that even this low edge of the shaded region exceeds constant star formation rate efficiency model predictions at $z \sim 10$ suggests that star formation in the early universe may be much more efficient than suggested in many analyses with HST and ground-based data (Bouwens et al. 2015, 2021; Harikane et al. 2018, 2022b; Oesch et al. 2018; Tacchella et al. 2018; Stefanon et al. 2021, 2022b). Differences with the constant star formation efficiency models are even more substantial at $z \geq 13$.

to Naidu et al. (2022a). In general, there is broad similarity in all LF results obtained to the present with $JWST$, given the limited statistics available and thus large uncertainties.

4.2 UV LF Results from Our Literature Samples

As an alternative to direct determinations of the UV LF from our own selections of $z \geq 8$ candidates, we also consider the use of the literature results we analyzed and characterized in (§3.3) to derive UV LF results at $z \sim 10$, $z \sim 13$, and $z \sim 17$.

As we have already noted, large numbers of $z \geq 9$ candidate galaxies have been identified in various analyses of the early NIRCам data, and the purpose of this analysis is to show the implications of these results for the $z \geq 9$ UV LFs assuming that a significant fraction of these candidates are at $z \geq 9$.

It is interesting to derive the implied LF results as a function of the apparent robustness level of the candidates, to demonstrate how high the volume density of sources is even including only the best candidates. We take the UV luminosity of individual candidates to the values we measure based on our own photometry. A complete list of the candidates we utilize and their classification into the groups defined in (§3.3) is provided in Tables 3 and B1-B5.

Given the diverse selection criteria used to construct these literature LFs, we take the selection volume to be equal to the *detection* volume, as we very conservatively assume that all *detected* sources are *selectable* by one or more of the diverse selection criteria used in the literature. By making this assumption, our derived LFs should

be as low as possible given the available selection volume at high redshift.

To illustrate the implications of including all of the published $z \geq 8$ candidates to the present in LF determinations, we present $z \sim 10$, $z \sim 13$, and $z \sim 17$ LF results in Figure 5 using the solid grey circles and error bars. For clarity, UV LF and luminosity density results derived for this “possible” sample and later for the “solid” literature sample also include the full set of sources from the “solid”+“robust” and “robust” samples, respectively. Gray lines are drawn connecting the grey points to help the literature LF results. Those LF results are some ~ 2 - $10\times$ higher than the LF results reported by Donnan et al. (2022), Harikane et al. (2022a), Bouwens et al. (2022b), and Finkelstein et al. (2022b) over the luminosity range -20 to -18 mag. One explanation is that this full sample includes sources we have graded as “possible”, which we estimate to have a lower probability of being at $z > 8$.

Thus, one reason these LFs might be so much in excess of the individual LF determinations is because the list of “possible” $z > 8$ candidates (Table B3-B5) include large numbers of lower-redshift interlopers. This motivates us to also derive LF results based on candidates which satisfy much more stringent quality requirements, such as those that make up our “solid” or “robust” sample of sources from the literature.

Results for the “solid” and “robust” samples are shown in Figures 6 with the partially transparent pink and red points, respectively. Even the $z \sim 10$ LF results from the “solid” candidates exceed the results from Donnan et al. (2022) and Harikane et al. (2022a) by factors

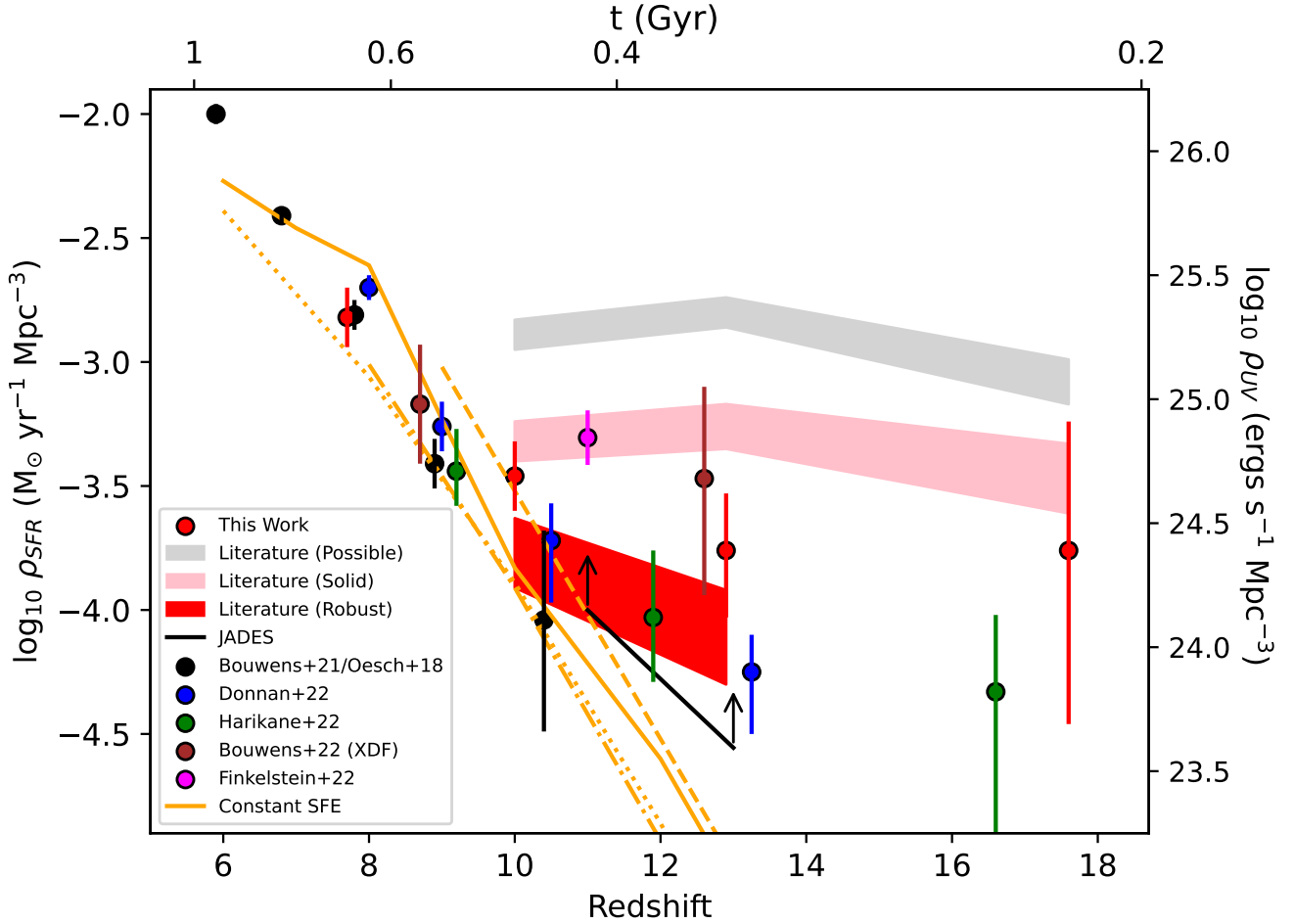


Figure 7. *UV* luminosity and star formation rate density integrated to -19 mag. Shown are determinations from the present analysis (*red circles*), [Donnan et al. \(2022\)](#) (*blue circles*), [Harikane et al. \(2022a\)](#) (*green circles*), [Bouwens et al. \(2022b\)](#) (*brown circles*), [Finkelstein et al. \(2022b\)](#) (*magenta circles*), and [Bouwens et al. \(2021\)/Oesch et al. \(2018\)](#) (*black circles*). The solid black line and lower limits are the *UV* luminosity densities we compute brightward of -19 mag from the spectroscopically-confirmed sources presented in [Robertson et al. \(2022\)](#); [Curtis-Lake et al. \(2022\)](#). The light gray, pink, and red shaded regions give the *UV* luminosity densities at $z \sim 10$ – 17 inferred based on literature candidates graded here as “robust,” “solid,” and “possible,” respectively. The reason the latter two regions are 3 – $7\times$ and 8 – $20\times$ higher, respectively, in luminosity density than inferred by some analyses in the literature, e.g., [Donnan et al. \(2022\)](#) and [Harikane et al. \(2022a\)](#), is due to many analyses only including a fraction of the potentially credible $z \geq 8$ candidates from the literature (which are here graded as “solid” or “possible”). The orange lines indicate the expected evolution in the *UV* luminosity density assuming no evolution in the star formation efficiency of galaxies across cosmic time using the models of [Mason et al. \(2015\)](#) (*solid*), [Tacchella et al. \(2018\)](#) (*dot-dashed*), [Bouwens et al. \(2021\)](#) (*dotted*), and [Harikane et al. \(2022b\)](#) (*dashed*).

of ~ 1.5 to 2 , but agree better with our own results and those of [Finkelstein et al. \(2022b\)](#). At $z \sim 13$ and $z \sim 17$, the LF results derived from the “solid” candidates lies even more clearly in excess of the LF results from [Donnan et al. \(2022\)](#), [Harikane et al. \(2022a\)](#), and our own analysis.

Given current uncertainties over what fraction of current $z \geq 9$ candidate lists are bona-fide, we express the LF results we derive from the literature in Table 8 in terms of a region spanning the range between our LF results using the “robust” candidates and the candidates we classify as “solid.” These results are also shown in Figure 6, and we can see it easily encompasses the range of LF results reported in various studies.

5 DISCUSSION

5.1 Evolution of Star-Forming Galaxies from $z \sim 17$ to $z \sim 8$

There has been a lot of discussion over the last ten years regarding how much star formation took place during the earliest epochs of the universe, when $z > 10$. Some of this discussion had been based on the evolution of the *UV* LF at $z > 6$ and debate between a slower evolution in the apparent SFR and *UV* luminosity density (e.g., [McLeod et al. 2016](#)) and a more rapid evolution (e.g., [Oesch et al. 2014, 2018](#); [Bouwens et al. 2021](#)).

The relatively small number of apparently robust $z \sim 10$ candidates identified in the wider area data searched by [Oesch et al. \(2018\)](#) seemed to weigh in favor of a faster evolution. Nevertheless, the apparent discovery of many luminous galaxy candidates (particularly now with *JWST*) in the $z \geq 9$ universe over wide areas (e.g., [Bowler et al. 2020](#); [Roberts-Borsani et al. 2022](#); [Harikane et al. 2022b](#); [Finkelstein et al. 2022c](#); [Bagley et al. 2022](#); [Kauffmann et al. 2022](#);

Table 9. Inferred *UV* Luminosity Densities¹ at $z \geq 8$

Redshift	ρ_{UV} [$\text{ergs s}^{-1} \text{Mpc}^{-3}$]	ρ_{SFR} [$M_{\odot}/\text{yr}/\text{Mpc}^3$]
Direct Determinations		
8	$25.21^{+0.28}_{-0.28}$	$-2.94^{+0.28}_{-0.28}$
10.0	$24.69^{+0.14}_{-0.14}$	$-3.46^{+0.14}_{-0.14}$
12.9	$24.39^{+0.23}_{-0.23}$	$-3.76^{+0.23}_{-0.23}$
17.6	$24.39^{+0.52}_{-0.70}$	$-3.76^{+0.52}_{-0.70}$
“Robust” Literature Sample		
10	24.38 ± 0.14	-3.77 ± 0.14
13	24.04 ± 0.19	-4.11 ± 0.19
“Solid” Literature Sample		
10	24.83 ± 0.08	-3.32 ± 0.08
13	24.89 ± 0.09	-3.26 ± 0.09
17	24.68 ± 0.14	-3.47 ± 0.14
“Possible” Literature Sample		
10	25.26 ± 0.06	-2.89 ± 0.06
13	25.35 ± 0.06	-2.80 ± 0.06
17	25.07 ± 0.09	-3.08 ± 0.09

¹ Luminosity densities integrated down to -19 mag.

Donnan et al. 2022) and the discovery of apparent Balmer breaks in galaxies at $z \geq 9$ (Zheng et al. 2012; Hashimoto et al. 2018) pointed in the other direction, towards more substantial early star formation activity.

A good baseline for evaluating early star formation activity is through comparison with the predictions of constant star formation efficiency models (SFE). Already, such models have succeeded in providing a plausible baseline for modeling star formation across cosmic time (e.g. Mason et al. 2015; Bouwens et al. 2015, 2021; Mashian et al. 2016; Harikane et al. 2018, 2022b; Oesch et al. 2018; Tacchella et al. 2018; Stefanon et al. 2021, 2022b). While there have been a large number of models using the constant SFE assumption to model the evolution of the SFR density across cosmic time, we will test the results against only four: Mason et al. (2015), Bouwens et al. (2015), Tacchella et al. (2018), and Harikane et al. (2022b).

A comparison of the constant star formation efficiency model results are shown in Figure 6. As in other recent studies, the evolution on the *UV* LF appears to be significantly in excess of that predicted from constant SFE models at $z \geq 12$ (for galaxies more luminous than ~ -19). Not only does this clearly appear to be the case for all LF determinations at $z \geq 11$, but it is even true if we only make use of sources from the literature that we classify as robust. If one or more of the candidate $z \sim 17$ galaxies is actually at such a high redshift (Donnan et al. 2022; Harikane et al. 2022a; Naidu et al. 2022b; but see also Zavala et al. 2022; Naidu et al. 2022b), differences with the constant SFE models is even larger.

It is unclear whether this indicates the SFE of galaxies is indeed more efficient or if the IMF of (luminous) galaxies is very different at early times. If the stellar masses in $z > 8$ galaxies are as high as found in Labbé et al. (2022), it would argue in favor of a substantially higher SFE. There is clearly a limit to how high the SFE can be based on the baryon mass in collapsed halos at $z > 8$, and interestingly enough, both Boylan-Kolchin (2022) and Naidu et al. (2022b) find that some galaxies may be in violation of these limits. Potential resolution of this enigma could include an evolution in the stellar IMF in star-

forming galaxies at $z > 8$ such that the mass-to-light ratio in early galaxies is substantially lower than at later times in the history of the universe (e.g. Steinhardt et al. 2022; Harikane et al. 2022a; Inayoshi et al. 2022).

5.2 *UV* Luminosity and SFR Densities of Galaxies at $z \geq 8$

An alternate way of assessing the star formation activity in the early universe is by looking at results in terms of the *UV* luminosity density and SFR density. In characterizing the evolution, we only consider sources and *UV* LF results brighter than -19 mag to avoid extrapolating the LF faintward of what can be well probed with early *JWST* data, i.e., ~ 29 mag, as used both in the present study, Donnan et al. (2022), and Finkelstein et al. (2022b).

We have adopted such a limit to avoid substantial extrapolations of *UV* LF results to much fainter luminosities where they are less well constrained. If we consider extrapolations to -17 mag (as considered in both Donnan et al. 2022 and Harikane et al. 2022a), $z \sim 17$ SFR density results derived assuming a faint-end slope α of -2.1 (as assumed by Harikane et al. 2022a) vs. assuming a faint-end slope of -3 (as predicted at $z \sim 17$ by Mason et al. 2015) differ by ~ 1 dex. Given that difference would then be driven entirely by the assumed faint-end slope, it is clearly preferable to quote SFR density results only to luminosity limits which are well probed by the observations.

In Figure 7, we present our results for the *UV* luminosity density evolution both from our direct LF analyses. Additionally, we include the equivalent SFR density results, assuming the conversion factor \mathcal{K}_{FUV} is $0.7 \times 10^{-29} M_{\odot} \text{ year}^{-1} \text{ erg}^{-1} \text{ s Hz}$ from Madau & Dickinson (2014), which assumes a Chabrier (2003) IMF, a constant star formation rate, and metallicity $Z = 0.002 Z_{\odot}$. For context, we also include the results obtained by several other analyses of the *JWST* observations (Donnan et al. 2022; Harikane et al. 2022a; Finkelstein et al. 2022b) and also several constant star formation efficiency (SFE) predictions for the *UV* luminosity density evolution (Mason et al. 2015; Tacchella et al. 2018; Bouwens et al. 2021; Harikane et al. 2022b).

In Figure 7, we also show the *UV* luminosity density results derived from our literature samples of the same fields. Separate results are presented for candidates categorized as “robust,” “solid,” and “possible” with the shaded red, pink, and grey regions, respectively. For additional reference, we include as a solid black line and upward arrows the implied lower limits on the *UV* luminosity densities at $z > 10$ based on the recent *JWST* ADvanced Extragalactic Survey (JADES) spectroscopic results over the HUDF/XDF region (Robertson et al. 2022; Curtis-Lake et al. 2022). For those limits, we adopt the *UV* luminosities measured by Robertson et al. (2022) and assume a total search area of $2 \times (1.5 \text{ arcmin})^2$ and that sources can be selected over the entire volume $z = 10-12$ and $z = 12-14$.

It is striking how much higher the implied luminosity densities of the “possible” candidates are relative to the results derived from those candidates in the other categories. Results including all of the candidates are $\sim 3\times$ and $\sim 8\times$ higher than those candidates we grade as “solid” and “robust,” respectively, at $z \sim 10$ and $\sim 7\times$ and $\sim 20\times$, respectively, higher at $z \geq 12$. These same *UV* luminosity density results are also significantly in excess of our own *UV* luminosity density results as well as the results of Donnan et al. (2022), Harikane et al. (2022a), and Finkelstein et al. (2022b).

Clearly, much of the excess could be due to the presence of potentially substantial numbers of lower-redshift contaminants in various $z \geq 8$ selections. The detection of possibly significant flux blueward of the breaks in the median stacks of the “possible” candidates is indeed suggestive of such a conclusion (cf., §3.3, Appendix C).

There are clearly large uncertainties in what fraction of these fainter sources are at high redshifts. As we demonstrate in Appendix E, the assessment of the reliability of specific $z \geq 8$ candidates can vary substantially between the different studies. It is indicative of the challenges with these early data sets that our independent evaluation of the candidates from [Donnan et al. \(2022\)](#), [Harikane et al. \(2022a\)](#), [Finkelstein et al. \(2022b\)](#), and our own selections place a non-negligible fraction of these candidates ($\geq 20\%$) in our lowest quality bin (Table 4).

Meanwhile, results using the “robust” candidates appear to be in excellent agreement with the collective LF results of [Donnan et al. \(2022\)](#) and [Harikane et al. \(2022a\)](#), while our own results and those of [Finkelstein et al. \(2022b\)](#) agree better with the results obtained using the “solid” candidates. The [Finkelstein et al. \(2022b\)](#) LF results appear to be $\approx 2\times$ higher than the [Donnan et al. \(2022\)](#) results due to the $\sim 2\times$ higher completeness of the [Finkelstein et al. \(2022b\)](#) selection to “robust”+“solid” $z \geq 8$ candidates from the literature (Table 4).⁴

Without spectroscopy, it is difficult to know which of these two results is more reliable. A key question is the extent to which sources in our “solid” literature sample are at $z > 8$. Simulation results from both [Harikane et al. \(2022a\)](#) and [Larson et al. \(2022\)](#) indicate that $z \geq 8$ selections over CEERS-like data sets might well include an appreciable number of lower-redshift interlopers, even restricting such selections to sources with $> 80\%$ of the integrated likelihood at $z > 5.5$ (as is required for sources that make up our “solid” literature selections). Based on the expected contamination in the first *JWST* fields (likely due to the limited depth of the data blueward of the break), [Harikane et al. \(2022a\)](#) require that $z \geq 9$ candidates satisfy an especially demanding $\Delta(\chi^2(z_{\text{low}}) - \chi^2(z_{\text{high}})) > 9$ selection criterion to be included in their high-redshift samples.

Another concerning aspect of sources in our “solid” literature selections is the much more limited overlap between candidates reported in different studies. While 90% of the $z \geq 9$ candidates in our “robust” literature selections are identified as part of multiple studies, only 26% of the $z \geq 9$ candidates in the “solid” literature selections are found in multiple studies.⁵ This suggests that a larger percentage of sources in our “solid” literature sample may in fact be lower redshift contaminants, but it is a huge open question what that percentage is.

Even median stacking of the SED results is of little use in ascertaining whether sources in our “solid” literature selections are reliable. As we show in Appendix C, very similar stack results are obtained using either the “robust” or “robust”+“solid” subsamples of literature candidates. In both cases, a pronounced ~ 1.5 -mag spectral break is seen, with no significant flux blueward of the break. Also both stacks reveal a blue spectral slope redward of the break.

Regardless of what the actual SFR density is at $z \geq 10$, i.e., whether it is closer to the “robust” or “solid” literature results shown in Figure 7, essentially all of the present results lie in significant excess of the constant SFE models ([Mason et al. 2015](#); [Tacchella](#)

[et al. 2018](#); [Bouwens et al. 2021](#); [Harikane et al. 2022b](#)) by factors of ~ 2 -6 at $z \sim 12$ and by even larger factors at $z > 12$. There have been a variety of different explanations offered for this deviation from the constant SFE predictions in the literature. One possibility has been to suppose that the mass-to-light ratios of galaxies in the early universe are much lower than at later points in cosmic time, which could result from a change in the effective IMF of galaxies in the $z > 10$ universe to one which is much more top heavy (e.g. [Harikane et al. 2022a](#); [Steinhardt et al. 2022](#); [Inayoshi et al. 2022](#)).

Other possibilities have included the hypothesis perhaps AGN contribute much more significant to the light from the earliest generation of galaxies (e.g. [Harikane et al. 2022a](#)), there is much greater scatter in the star formation rates in galaxies in the early universe away from the main star-forming sequence (e.g. [Mason et al. 2022](#)), as well as a number of other explanations (e.g. [Ferrara et al. 2022](#); [Mirocha & Furlanetto 2022](#); [Harikane et al. 2022a](#); [Kannan et al. 2022](#)). Ascertaining which of these explanations is correct will ultimately require an extensive amount of follow-up observations with ALMA and *JWST*, especially involving spectroscopy as e.g. the recent confirmation of a $z = 9.76$ source and $z > 10$ sources by JADES team demonstrates ([Roberts-Borsani et al. 2022](#); [Curtis-Lake et al. 2022](#); [Robertson et al. 2022](#)).

6 SUMMARY

We have derived luminosity functions, and set constraints on the UV luminosity and SFR density from $z \sim 8$ to $z \sim 17$, using the three most well-studied *JWST* NIRCcam data sets from the first 5 months of *JWST* science operations, namely, the SMACS0723 cluster field ([Pontoppidan et al. 2022](#)), the GLASS Abell 2744 parallel field ([Treu et al. 2022](#)), and four CEERS ([Finkelstein et al. 2022b](#)) extragalactic fields.

We have selected of samples of $z \sim 8$, $z \sim 10$, $z \sim 13$, and $z \sim 17$ galaxies in these fields, and made full use of the very extensive selections done by others to date. In particular, we have investigated the challenges of the selection of $z \geq 8$ galaxies and derivation of UV LF results from these early *JWST* NIRCcam observations. Even with a very conservative approach to selections, both from our own and similarly sub-selecting those of other studies, we find that luminous galaxies in the first 400-500 Myr are as enigmatic as the first *JWST* results suggested.

We first make use of two different reductions of the NIRCcam observations to test the sensitivity of $z \geq 8$ selections to the reduction technique. The first set of reductions we utilize relies on the GRIZLI NIRCcam pipeline, while the second leverages an alternate set of reductions made with the PENCIL NIRCcam pipeline. Both reductions take advantage of advances made in the calibrations of the NIRCcam zeropoints, as well as including steps to minimize the impact of $1/f$ noise and “snowball” artefacts.

Based on these reductions, we construct substantial samples of nominally $z \sim 8$, $z \sim 10$, $z \sim 13$, and $z \sim 17$ galaxies using two color Lyman-break selection criteria. Our redshift selection functions indicate that our selections cover redshift ranges of $z \sim 7 - 9$, $z \sim 9 - 11$, $z \sim 12 - 14$, and $z \sim 16 - 19$. Our primary selection using the GRIZLI reductions includes 18 $z \sim 8$, 12 $z \sim 10$, 5 $z \sim 13$, and 1 $z \sim 17$ galaxies, while our alternate selection using the PENCIL reductions yields 22 $z \sim 8$, 13 $z \sim 10$, 3 $z \sim 13$, and 1 $z \sim 17$ galaxy candidates. The overlap between these samples, even from two recent reductions, is only ~ 40 -50%, indicative of the subtleties and challenges of identifying sources at high redshift.

Using sources from the above selection and using estimates of the

⁴ We remark in passing that the [Finkelstein et al. \(2022b\)](#) LF results appears to be more consistent than with the empirical completeness estimates we derive on the basis our literature selections (Table 4) than is the case for either the [Donnan et al. \(2022\)](#) or [Harikane et al. \(2022a\)](#) analyses where the completeness of their selections (Table 5) is $\sim 2\times$ lower than assumed in their LF analyses.

⁵ For reference, the percentage of $z \geq 9$ candidates from our “possible” literature selections that occur in more than one study is just 5%. This demonstrates there is really a difference in the quality of the candidates that make up of our literature subsamples.

selection volumes in our search fields, we have derived estimates of the UV LF at $z \sim 8$, $z \sim 10$, $z \sim 13$, and $z \sim 17$. While the uncertainties are still very large, our UV LF results are suggestive of factors of 6 and 6 decreases in the normalization of the UV LF from $z \sim 8$ to $z \sim 13$ and $z \sim 17$, respectively. Not surprisingly, the results we obtain are similar to the relatively mild evolution in the UV luminosity density already reported in Naidu et al. (2022a), Donnan et al. (2022), Harikane et al. (2022a), Bouwens et al. (2022b), and Finkelstein et al. (2022b).

We also take these results and set constraints on the UV luminosity and SFR density from $z \sim 17$ to $z \sim 8$ for galaxies more luminous than -19 mag. Similar to what we found for the UV LF results, the UV luminosity density and SFR density, both our direct determinations and the results based on likely robust $z \sim 11$ -13 candidates from the literature, lie significantly in excess of the constant star formation efficiency (SFE) models, by factors of ~ 2 -6. Interpretation of these results is unclear, and it is open question whether the new results indicate the SFE of galaxies is indeed more efficient or if the IMF of (luminous) galaxies is very different at early times.

As a complement to direct determinations of the UV LF at $z \geq 8$, we also derive UV LF and luminosity density results, by taking advantage of the full samples of $z \sim 10$, $z \sim 13$, and $z \sim 17$ galaxies that have been identified to date over the three most well studied fields. We then segregate this sample of candidates into three different samples "robust," "solid," and "possible" based on how likely sources are to be at $z > 5.5$ based on our photometry of the sources in both our fiducial and secondary reductions of the NIRC*am* imaging observations.

We first considered the luminosity densities we would derive including all $z \geq 8$ candidates reported over the three most studied fields to the present. Remarkably, we find a $10\times$ and $30\times$ higher luminosity densities at $z \geq 12$ relying on the "solid" and "possible" candidates than relying on the "robust" candidates from the literature alone. These results demonstrate how uncertain the luminosity densities are at $z > 6$ and how much the results depend on the extent to what lower-redshift sources contaminate the $z \geq 8$ selections.

Even allowing for a substantial amount of contamination in our selections of "possible" $z \geq 8$ sources from the literature, large (~ 0.5 -1.0 dex: factors of 3 to 10) differences exist between the luminosity density results derived from sources graded "robust" and those graded "solid." If the bulk of the $z \geq 10$ candidates graded "solid" are instead at lower redshift, the true luminosity density results at $z \geq 10$ would be more along the lines of what has been found by Donnan et al. (2022) and Harikane et al. (2022a), which are consistent with the recent spectroscopic results of Curtis-Lake et al. (2022) and closer to the predictions of the constant SFE models. Some of the recent simulation results from Harikane et al. (2022a) and Larson et al. (2022) are suggestive of at least modest levels of contamination in the first JWST $z \geq 8$ selections with NIRC*am*.

On the other hand, if the bulk of the $z \geq 8$ candidates graded "solid" are bona-fide, then the UV LFs and UV luminosity density at $z \sim 10$ and $z \geq 12$ could be up to $\sim 3\times$ and $\sim 7\times$ higher and more in the range of the LF results we derive from our own selection of $z \geq 8$ sources and also more consistent with the results of Finkelstein et al. (2022b). Supportive of these high luminosity density results are the median stack results we obtain for our selection of "solid" candidates from the literature, which appear to have almost identical characteristics to what we obtain from a similar stack of "robust" candidates from the literature.

Whatever the reality is, it is clear that huge open question remain regarding the true UV LF and UV luminosity density results at $z \geq 8$. To resolve these open questions, deeper imaging observations

and follow-up spectroscopy with JWST NIRSpec and the grisms will be required, allowing for a significantly improved reliability of $z \geq 8$ selections and UV LF determinations going forwards. Fortunately, there are already significant on-going efforts obtaining sensitive imaging over fields like the HUDF (e.g. Bouwens et al. 2022b; Robertson et al. 2022) and sensitive spectroscopic campaigns by the substantial JADES program (e.g. Curtis-Lake et al. 2022) that provide the needed new data.

ACKNOWLEDGEMENTS

RJB acknowledges support from NWO grants 600.065.140.11N211 (vrijcompetitie) and TOP grant TOP1.16.057. MS acknowledges support from the CIDEAGENT/2021/059 grant, from project PID2019-109592GB-I00/AEI/10.13039/501100011033 from the Spanish Ministerio de Ciencia e Innovación - Agencia Estatal de Investigación, and from Proyecto ASFAE/2022/025 del Ministerio de Ciencia y Innovación en el marco del Plan de Recuperación, Transformación y Resiliencia del Gobierno de España RPN acknowledges funding from JWST programs GO-1933 and GO-2279. Support for this work was provided by NASA through the NASA Hubble Fellowship grant HST-HF2-51515.001-A awarded by the Space Telescope Science Institute, which is operated by the Association of Universities for Research in Astronomy, Incorporated, under NASA contract NAS5-26555. PAO acknowledges support from: the Swiss National Science Foundation through project grant 200020 207349. The Cosmic Dawn Center (DAWN) is funded by the Danish National Research Foundation under grant No. 140. This work is based on observations made with the NASA/ESA/CSA James Webb Space Telescope. The data were obtained from the Mikulski Archive for Space Telescopes at the Space Telescope Science Institute, which is operated by the Association of Universities for Research in Astronomy, Inc., under NASA contract NAS 5-03127 for JWST.

DATA AVAILABILITY

All data used here are available from the Barbara A. Mikulski Archive for Space Telescopes (MAST: <https://mast.stsci.edu>), both in the form of raw and high level science products.

REFERENCES

- Adams N. J., et al., 2022, arXiv e-prints, p. [arXiv:2207.11217](https://arxiv.org/abs/2207.11217)
- Anders P., Fritze-v. Alvensleben U., 2003, *A&A*, **401**, 1063
- Atek H., et al., 2022, arXiv e-prints, p. [arXiv:2207.12338](https://arxiv.org/abs/2207.12338)
- Bagley M. B., et al., 2022, arXiv e-prints, p. [arXiv:2205.12980](https://arxiv.org/abs/2205.12980)
- Beckwith S. V. W., et al., 2006, *AJ*, **132**, 1729
- Bertin E., Arnouts S., 1996, *A&AS*, **117**, 393
- Bhatawdekar R., Conselice C. J., Margalef-Bentabol B., Duncan K., 2019, *MNRAS*, **486**, 3805
- Bouwens R. J., et al., 2011, *ApJ*, **737**, 90
- Bouwens R. J., et al., 2015, *ApJ*, **803**, 34
- Bouwens R. J., et al., 2016, *ApJ*, **830**, 67
- Bouwens R. J., Stefanon M., Oesch P. A., Illingworth G. D., Nanayakkara T., Roberts-Borsani G., Labbé I., Smit R., 2019, *ApJ*, **880**, 25
- Bouwens R. J., et al., 2021, *AJ*, **162**, 47
- Bouwens R. J., Illingworth G. D., Ellis R. S., Oesch P. A., Stefanon M., 2022a, arXiv e-prints, p. [arXiv:2205.11526](https://arxiv.org/abs/2205.11526)
- Bouwens R. J., et al., 2022b, arXiv e-prints, p. [arXiv:2211.02607](https://arxiv.org/abs/2211.02607)
- Bowler R. A. A., et al., 2015, *MNRAS*, **452**, 1817

- Bowler R. A. A., Jarvis M. J., Dunlop J. S., McLure R. J., McLeod D. J., Adams N. J., Milvang-Jensen B., McCracken H. J., 2020, *MNRAS*, **493**, 2059
- Boylan-Kolchin M., 2022, arXiv e-prints, [p. arXiv:2208.01611](https://arxiv.org/abs/2208.01611)
- Brammer G. B., van Dokkum P. G., Coppi P., 2008, *ApJ*, **686**, 1503
- Brammer G., Strait V., Matharu J., Momcheva I., 2022, grizli, Zenodo, [doi:10.5281/zenodo.6672538](https://doi.org/10.5281/zenodo.6672538)
- Castellano M., et al., 2022, arXiv e-prints, [p. arXiv:2207.09436](https://arxiv.org/abs/2207.09436)
- Chabrier G., 2003, *PASP*, **115**, 763
- Coleman G. D., Wu C. C., Weedman D. W., 1980, *ApJS*, **43**, 393
- Cullen F., et al., 2022, arXiv e-prints, [p. arXiv:2208.04914](https://arxiv.org/abs/2208.04914)
- Curtis-Lake E., et al., 2022, arXiv e-prints, [p. arXiv:2212.04568](https://arxiv.org/abs/2212.04568)
- Donnan C. T., et al., 2022, arXiv e-prints, [p. arXiv:2207.12356](https://arxiv.org/abs/2207.12356)
- Duncan K., et al., 2014, *MNRAS*, **444**, 2960
- Dunlop J. S., et al., 2013, *MNRAS*, **432**, 3520
- Ferrara A., Pallottini A., Dayal P., 2022, arXiv e-prints, [p. arXiv:2208.00720](https://arxiv.org/abs/2208.00720)
- Finkelstein S. L., et al., 2013, *Nature*, **502**, 524
- Finkelstein S. L., et al., 2015, *ApJ*, **810**, 71
- Finkelstein S. L., et al., 2022a, arXiv e-prints, [p. arXiv:2207.12474](https://arxiv.org/abs/2207.12474)
- Finkelstein S. L., et al., 2022b, arXiv e-prints, [p. arXiv:2211.05792](https://arxiv.org/abs/2211.05792)
- Finkelstein S. L., et al., 2022c, *ApJ*, **928**, 52
- Furtak L. J., Atek H., Lehnert M. D., Chevallard J., Charlot S., 2021, *MNRAS*, **501**, 1568
- Grazian A., et al., 2015, *A&A*, **575**, A96
- Harikane Y., et al., 2018, *PASJ*, **70**, S11
- Harikane Y., et al., 2022a, arXiv e-prints, [p. arXiv:2208.01612](https://arxiv.org/abs/2208.01612)
- Harikane Y., et al., 2022b, *ApJS*, **259**, 20
- Hashimoto T., et al., 2018, *Nature*, **557**, 392
- Illingworth G. D., et al., 2013, *ApJS*, **209**, 6
- Inayoshi K., Harikane Y., Inoue A. K., Li W., Ho L. C., 2022, *ApJ*, **938**, L10
- Jiang L., et al., 2021, *Nature Astronomy*, **5**, 256
- Kannan R., et al., 2022, arXiv e-prints, [p. arXiv:2210.10066](https://arxiv.org/abs/2210.10066)
- Kauffmann O. B., et al., 2022, arXiv e-prints, [p. arXiv:2207.11740](https://arxiv.org/abs/2207.11740)
- Kikuchihara S., et al., 2020, *ApJ*, **893**, 60
- Kotulla R., Fritze U., Weibacher P., Anders P., 2009, *MNRAS*, **396**, 462
- Kron R. G., 1980, *ApJS*, **43**, 305
- Labbé I., et al., 2022, arXiv e-prints, [p. arXiv:2207.12446](https://arxiv.org/abs/2207.12446)
- Larson R. L., et al., 2022, arXiv e-prints, [p. arXiv:2211.10035](https://arxiv.org/abs/2211.10035)
- Lucy L. B., 1974, *AJ*, **79**, 745
- Madau P., Dickinson M., 2014, *ARA&A*, **52**, 415
- Mashian N., Oesch P. A., Loeb A., 2016, *MNRAS*, **455**, 2101
- Mason C. A., Trenti M., Treu T., 2015, *ApJ*, **813**, 21
- Mason C. A., Trenti M., Treu T., 2022, arXiv e-prints, [p. arXiv:2207.14808](https://arxiv.org/abs/2207.14808)
- McLeod D. J., McLure R. J., Dunlop J. S., 2016, *MNRAS*, **459**, 3812
- McLure R. J., et al., 2013, *MNRAS*, **432**, 2696
- Mirocha J., Furlanetto S. R., 2022, arXiv e-prints, [p. arXiv:2208.12826](https://arxiv.org/abs/2208.12826)
- Naidu R. P., et al., 2022a, arXiv e-prints, [p. arXiv:2207.09434](https://arxiv.org/abs/2207.09434)
- Naidu R. P., et al., 2022b, arXiv e-prints, [p. arXiv:2208.02794](https://arxiv.org/abs/2208.02794)
- Oesch P. A., et al., 2014, *ApJ*, **786**, 108
- Oesch P. A., et al., 2015, *ApJ*, **804**, L30
- Oesch P. A., et al., 2016, *ApJ*, **819**, 129
- Oesch P. A., Bouwens R. J., Illingworth G. D., Labbé I., Stefanon M., 2018, *ApJ*, **855**, 105
- Oke J. B., Gunn J. E., 1983, *ApJ*, **266**, 713
- Ono Y., et al., 2012, *ApJ*, **744**, 83
- Ono Y., et al., 2022, arXiv e-prints, [p. arXiv:2208.13582](https://arxiv.org/abs/2208.13582)
- Pontoppidan K. M., et al., 2022, *ApJ*, **936**, L14
- Reddy N. A., Steidel C. C., 2009, *ApJ*, **692**, 778
- Richardson W. H., 1972, *Journal of the Optical Society of America* (1917-1983), **62**, 55
- Rigby J., et al., 2022, arXiv e-prints, [p. arXiv:2207.05632](https://arxiv.org/abs/2207.05632)
- Roberts-Borsani G., Morishita T., Treu T., Leethochawalit N., Trenti M., 2022, *ApJ*, **927**, 236
- Robertson B. E., et al., 2022, arXiv e-prints, [p. arXiv:2212.04480](https://arxiv.org/abs/2212.04480)
- Schenker M. A., et al., 2013, *ApJ*, **768**, 196
- Schlafly E. F., Finkbeiner D. P., 2011, *ApJ*, **737**, 103
- Song M., et al., 2016, *ApJ*, **825**, 5
- Stark D. P., Ellis R. S., Chiu K., Ouchi M., Bunker A., 2010, *MNRAS*, **408**, 1628
- Stefanon M., et al., 2019, *ApJ*, **883**, 99
- Stefanon M., Bouwens R. J., Labbé I., Illingworth G. D., Gonz alez V., Oesch P. A., 2021, *ApJ*, **922**, 29
- Stefanon M., Bouwens R. J., Labbé I., Illingworth G. D., Gonz alez V., Oesch P. A., 2022a, arXiv e-prints, [p. arXiv:2206.13525](https://arxiv.org/abs/2206.13525)
- Stefanon M., Bouwens R. J., Labbé I., Illingworth G. D., Oesch P. A., van Dokkum P., Gonzalez V., 2022b, *ApJ*, **927**, 48
- Steidel C. C., Adelberger K. L., Gialvalisco M., Dickinson M., Pettini M., 1999, *ApJ*, **519**, 1
- Steidel C. C., Adelberger K. L., Shapley A. E., Pettini M., Dickinson M., Gialvalisco M., 2003, *ApJ*, **592**, 728
- Steinhardt C. L., Kokorev V., Rusakov V., Garcia E., Sneppen A., 2022, arXiv e-prints, [p. arXiv:2208.07879](https://arxiv.org/abs/2208.07879)
- Tacchella S., Bose S., Conroy C., Eisenstein D. J., Johnson B. D., 2018, *ApJ*, **868**, 92
- Topping M. W., Stark D. P., Endsley R., Plat A., Whitler L., Chen Z., Charlot S., 2022, arXiv e-prints, [p. arXiv:2208.01610](https://arxiv.org/abs/2208.01610)
- Treu T., et al., 2022, *ApJ*, **935**, 110
- Whitler L., Endsley R., Stark D. P., Topping M., Chen Zuyi and Charlot S., 2022, arXiv e-prints, [p. arXiv:2208.01599](https://arxiv.org/abs/2208.01599)
- Wilkins S. M., Bouwens R. J., Oesch P. A., Labbé I., Sargent M., Caruana J., Wardlow J., Clay S., 2016, *MNRAS*, **455**, 659
- Yan H., Ma Z., Ling C., Cheng C., Huang J.-s., Zitrin A., 2022, arXiv e-prints, [p. arXiv:2207.11558](https://arxiv.org/abs/2207.11558)
- Zavala J. A., et al., 2022, arXiv e-prints, [p. arXiv:2208.01816](https://arxiv.org/abs/2208.01816)
- Zheng W., et al., 2012, *Nature*, **489**, 406
- Zitrin A., et al., 2015, *ApJ*, **810**, L12

APPENDIX A: $Z \geq 8$ CANDIDATES IDENTIFIED IN OUR SECONDARY REDUCTIONS

As a test on the sensitivity of $z \geq 8$ selections to the NIRCам reductions utilized, we perform a second search for $z \geq 8$ galaxies but using reductions made with PENCIL (§2.1). 22 $z \sim 8$, 13 $z \sim 10$, 3 $z \sim 13$, and 1 $z \sim 17$ galaxies are identified in these reductions.

The coordinates, photometric redshifts, apparent magnitudes, and spectral break amplitudes of the $z \geq 8$ candidates we find are indicated in Table A1. Also presented is the difference between the minimum χ^2 found for $z > 5.5$ and $z < 5.5$ fits to the observed SEDs of the sources, the estimated likelihood that a candidate has a redshift in excess of 5.5, and any earlier studies who identified a given source as part of their $z \geq 8$ searches.

APPENDIX B: ASSESSMENTS OF $Z \geq 9$ CANDIDATES IN THE LITERATURE

Given the considerable uncertainties regarding both the identity and total number of high-quality $z \geq 9$ candidate galaxies that have been identified to present, we have performed independent photometry on $z \geq 8$ candidates reported in a large number of manuscripts, as described in §3.3. Use was made both of a reduction of the NIRCам imaging data with the GRIZLI and PENCIL pipelines. We then categorized these $z \geq 9$ candidates in three categories “robust,” “solid,” and “possible.”

The purpose of this appendix is to present candidates from the literature which we classify as “solid” and “possible.” Those classified as “robust” have already been tabulated in Table 3. We place those candidates in Tables B1-B2 and B3-B5, respectively.

Table A1. Selection of $z \sim 10$, $z \sim 13$, and $z \sim 17$ sources identified over three most studied imaging fields in early *JWST* NIRCam observations using the alternate set of NIRCam reductions PENCIL (§2.1).

ID	RA	DEC	z_{phot}	m_{UV} [mag]	Lyman Break [mag]	$\Delta\chi^2$	$p(z > 5.5)$	Lit ¹
$z \sim 8$ Selection								
GLASSP2Z-4041319253	00:14:04.139	-30:19:25.35	$6.7^{+0.1}_{-0.1}$	28.5 ± 0.3	> 2.0	-6.3	0.95	
GLASSP2Z-4027418404	00:14:02.741	-30:18:40.41	$6.7^{+0.1}_{-0.1}$	27.7 ± 0.1	1.8 ± 0.5	-15.2	0.999	B22
S0723Z-3068426486	07:23:06.843	-73:26:48.62	$6.9^{+0.1}_{-0.1}$	27.0 ± 0.1	1.9 ± 0.2	-12.7	0.997	
S0723Z-3154126292	07:23:15.413	-73:26:29.28	$7.0^{+0.1}_{-0.1}$	25.0 ± 0.1	2.1 ± 0.1	-6.2	0.951	
GLASSP2Z-4029818477	00:14:02.988	-30:18:47.77	$7.2^{+0.1}_{-0.1}$	28.5 ± 0.2	> 2.1	-6.2	0.984	
GLASSP1Z-3589121028	00:13:58.915	-30:21:02.80	$7.4^{+0.2}_{-0.2}$	28.6 ± 0.3	> 2.3	-11.2	0.998	B22
S0723Z-3053127492	07:23:05.311	-73:27:49.22	$7.4^{+0.3}_{-0.3}$	26.2 ± 0.1	2.8 ± 2.3	-7.7	0.984	
GLASSP1Z-4027520346	00:14:02.759	-30:20:34.68	$7.4^{+0.2}_{-0.2}$	27.9 ± 0.2	> 2.3	-15.6	1.0	B22
GLASSP1Z-4002221454	00:14:00.229	-30:21:45.46	$7.4^{+0.4}_{-0.3}$	28.3 ± 0.2	> 2.2	-6.1	0.976	
GLASSP1Z-3577921174	00:13:57.791	-30:21:17.43	$7.5^{+0.4}_{-0.3}$	26.8 ± 0.2	2.3 ± 1.9	-38.9	1.0	B22
GLASSP2Z-4018619113	00:14:01.860	-30:19:11.38	$7.5^{+0.4}_{-0.3}$	28.3 ± 0.2	> 2.0	-9.9	0.997	
GLASSP2Z-4011518065	00:14:01.152	-30:18:06.58	$7.5^{+0.4}_{-0.3}$	28.3 ± 0.2	> 2.1	-15.2	1.0	
GLASSP2Z-4005219093	00:14:00.520	-30:19:09.31	$7.5^{+0.4}_{-0.4}$	28.6 ± 0.3	> 2.0	-4.3	0.934	
S0723Z-3295626401	07:23:29.566	-73:26:40.18	$7.5^{+0.7}_{-0.6}$	27.7 ± 0.2	2.1 ± 1.0	-19.0	1.0	B22
S0723Z-3201526042	07:23:20.158	-73:26:04.28	$7.6^{+0.3}_{-0.3}$	26.4 ± 0.1	3.4 ± 2.5	-40.3	1.0	D22, At22, Ad22, B22
GLASSP1Z-4041221457	00:14:04.126	-30:21:45.77	$7.8^{+0.4}_{-0.5}$	27.5 ± 0.2	2.1 ± 1.6	-7.7	0.981	B22
GLASSP1Z-4020822000	00:14:02.082	-30:22:00.07	$7.8^{+0.5}_{-0.5}$	26.8 ± 0.2	> 2.4	-6.6	0.977	B22
GLASSP1Z-4041820257	00:14:04.187	-30:20:25.79	$7.8^{+0.3}_{-0.3}$	28.1 ± 0.2	> 2.3	-26.5	1.0	
GLASSP2Z-4012218476	00:14:01.224	-30:18:47.68	$8.0^{+0.4}_{-0.4}$	27.3 ± 0.2	> 2.2	-4.1	0.923	
GLASSP1Z-4062820397	00:14:06.286	-30:20:39.79	$8.0^{+0.4}_{-0.3}$	28.3 ± 0.1	> 2.5	-6.0	0.958	
S0723Z-3226926062	07:23:22.697	-73:26:06.23	$8.1^{+0.2}_{-0.2}$	25.9 ± 0.1	> 3.9	-49.8	1.0	D22, At22, Ad22, B22
GLASSP2Z-3553419246	00:13:55.345	-30:19:24.63	$8.6^{+0.2}_{-0.2}$	27.6 ± 0.1	> 3.0	-22.1	1.0	Le22
$z \sim 10$ Selection								
CEERSYJ-9494458188	14:19:49.446	52:58:18.89	$8.8^{+0.3}_{-0.4}$	28.0 ± 0.2	1.6 ± 2.2	-9.4	0.993	W22 (v1)
CEERSYJ-9193553160	14:19:19.358	52:53:16.01	$9.0^{+0.5}_{-0.5}$	28.2 ± 0.2	1.7 ± 1.5	-17.2	1.0	La22, F22
CEERSYJ-0012959481	14:20:01.290	52:59:48.13	$9.2^{+0.7}_{-0.7}$	27.6 ± 0.2	> 1.9	-1.5	0.896	F22, B22
CEERSYJ-9353350378	14:19:35.336	52:50:37.88	$9.3^{+0.9}_{-0.6}$	27.8 ± 0.2	1.7 ± 1.6	-8.4	0.982	D22, F22, W22, B22
GLASSP1YJ-4045920571	00:14:04.599	-30:20:57.10	$9.4^{+0.5}_{-0.4}$	28.6 ± 0.2	> 2.3	-3.4	0.885	
GLASSP1YJ-4016420474	00:14:01.649	-30:20:47.44	$9.6^{+0.4}_{-0.4}$	29.5 ± 0.4	> 2.2	-6.0	0.954	
CEERSYJ-9320850526	14:19:32.081	52:50:52.63	$9.6^{+0.6}_{-0.6}$	28.2 ± 0.2	2.0 ± 1.7	-1.6	0.859	
CEERSYJ-9132749268	14:19:13.277	52:49:26.89	$9.7^{+0.7}_{-0.6}$	28.2 ± 0.2	> 2.0	-4.9	0.962	
GLASSP1YJ-4043920397	00:14:04.398	-30:20:39.78	$9.7^{+0.6}_{-0.5}$	29.2 ± 0.2	> 2.2	-5.8	0.969	H22
CEERSYJ-9329250443	14:19:32.926	52:50:44.37	$10.1^{+0.6}_{-0.6}$	27.5 ± 0.2	> 2.1	-3.5	0.947	
GLASSP1YJ-4028522189	00:14:02.857	-30:22:18.92	$10.3^{+0.6}_{-0.5}$	26.6 ± 0.1	> 3.3	-33.7	1.0	N22, C22, D22, H22, B22
CEERSYJ-9006450120	14:19:00.643	52:50:12.00	$10.4^{+0.7}_{-0.7}$	28.0 ± 0.2	> 1.8	-7.7	0.99	W22
CEERSYJ-9240348289	14:19:24.032	52:48:28.97	$10.7^{+0.7}_{-0.8}$	28.0 ± 0.2	> 1.5	-9.2	0.992	D22, F22
$z \sim 13$ Selection								
CEERSH-9463556328	14:19:46.353	52:56:32.81	$11.9^{+0.4}_{-0.5}$	27.7 ± 0.2	1.5 ± 1.2	-9.1	0.993	D22, F22, H22, B22
GLASSP2H-3576218534	00:13:57.629	-30:18:53.43	$13.4^{+0.8}_{-0.8}$	28.1 ± 0.2	> 1.8	-11.3	0.999	B22
CEERSH-9220551139	14:19:22.054	52:51:13.94	$13.5^{+0.8}_{-0.9}$	27.6 ± 0.2	> 1.9	-3.4	0.94	
$z \sim 17$ Selection								
CEERSK-9394956349	14:19:39.491	52:56:34.90	$16.0^{+0.4}_{-0.2}$	26.3 ± 0.1	1.5 ± 0.1	-4.2	0.885	D22, F22, H22, N22, B22

¹ Ad22 = [Adams et al. \(2022\)](#), At22 = [Atek et al. \(2022\)](#), C22 = [Castellano et al. \(2022\)](#), D22 = [Donnan et al. \(2022\)](#), H22 = [Harikane et al. \(2022a\)](#), La22 = [Labbé et al. \(2022\)](#), N22 = [Naidu et al. \(2022a,b\)](#), W22 = [Whitler et al. \(2022\)](#), Y22 = [Yan et al. \(2022\)](#), B22 = This Work (fiducial reductions: see Table 2)

APPENDIX C: MEDIAN STACK OF $Z \geq 9$ CANDIDATES WITH VARIOUS QUALITY FLAGS

In evaluating the quality of $z \geq 9$ candidates from the literature, we place the candidates in three different categories “robust,” “solid,” and “possible” depending on the relative likelihood we estimate for these sources to lie at $z < 5.5$ or $z > 5.5$ using our own photometry (see §3.3 for how these sets are defined).

In order to interpret each of these designations and determine if

the differences are meaningful, we construct median stacks of flux in different passbands and for candidates in different categories. The results are presented in Table C1.

While the median stack results in the “robust” and “solid” categories show no significant flux blueward of the nominal spectral breaks in the $z \geq 8$ candidates, the median stack in the “possible” category does show tentative $1-1.5\sigma$ detections in each of bands blueward of the break. Additionally, the median stack results in the “robust” and “solid” category shows larger spectral breaks, i.e., > 1.8

Table B1. Sample of $z \sim 10$, $z \sim 13$, and $z \sim 17$ candidate that we deem to be “solid” using our own photometry on our fiducial NIRCcam reductions*

ID	RA	DEC	z_{phot}	M_{UV}	Break [mag]	$\Delta\chi^2$	$p(z > 5.5)$	Lit
Castellano et al. (2022)								
GHZ3	00:14:06.940	-30:21:49.72	9.3/11.3 $^{+0.4}_{-0.4}$	-20.8	>1.8, 0.7 \pm 2.4	-4.1, -1.3	0.862, 0.814	B22
GHZ4	00:14:03.291	-30:21:05.57	9.9/10.8 $^{+0.8}_{-1.1}$	-19.8	>1.2, >1.7	-5.5, -6.4	0.950, 0.987	H22
Adams et al. (2022)								
10234	07:22:39.597	-73:30:06.25	11.5/11.7 $^{+0.3}_{-0.2}$	-20.6	1.2 \pm 0.2, 1.3 \pm 0.3	-7.9, -10.6	0.971, 0.997	
Atek et al. (2022)								
SMACS_z12b	07:22:52.245	-73:27:55.47	12.3/12.9 $^{+0.9}_{-0.9}$	-20.0	2.2 \pm 2.4, >1.4	-4.8, -4.5	0.961, 0.938	Y22, B22
SMACS_z16b	07:22:39.416	-73:30:08.15	15.3/14.9 $^{+0.8}_{-0.7}$	-21.0	>1.7, >1.2	-6.4, -6.3	0.971, 0.952	B22
Donnan et al. (2022, v2)								
29274_4	14:19:27.385	52:51:46.92	8.9/10.7 $^{+3.3}_{-2.7}$	-18.4	>0.8, >1.3	-0.9, -2.1	0.857, 0.821	
1434_2	14:19:26.110	52:52:52.41	9.2/10.2 $^{+0.7}_{-0.6}$	-18.8	>1.4, >1.4	-3.6, -0.5	0.922, 0.688	
43866	07:23:25.597	-73:26:12.41	9.5/7.9 $^{+0.7}_{-0.8}$	-18.1	1.2 \pm 0.7, 1.5 \pm 0.4	-3.7, -2.2	0.958, 0.771	
5071	07:22:56.854	-73:29:23.48	9.5/8.3 $^{+1.7}_{-1.7}$	-18.0	0.3 \pm 0.8, 0.5 \pm 0.6	-2.1, -1.7	0.887, 0.794	
14391	07:22:47.724	-73:28:28.31	9.5/9.2 $^{+1.4}_{-2.0}$	-18.8	1.3 \pm 0.3, 1.9 \pm 0.7	-0.1, -6.3	0.576, 0.975	
12682	07:22:38.948	-73:28:30.37	9.6/8.9 $^{+1.3}_{-1.3}$	-18.9	>1.6, >1.7	-5.6, -6.7	0.985, 0.990	
15019	07:22:58.265	-73:28:19.53	9.7/8.7 $^{+1.5}_{-1.5}$	-18.7	>1.0, >1.3	-1.8, -1.3	0.870, 0.784	
6200	07:22:41.502	-73:29:10.61	9.8/8.9 $^{+1.4}_{-1.3}$	-18.5	>1.3, >1.4	-3.2, -3.3	0.932, 0.931	
3763	07:22:49.132	-73:29:31.17	9.9/8.0 $^{+1.0}_{-0.9}$	-19.0	2.0 \pm 1.5, >2.3	-0.2, -4.7	0.767, 0.978	
7606	07:22:29.557	-73:29:05.66	9.9/9.3 $^{+1.4}_{-1.5}$	-18.1	>0.7, >0.6	-3.8, -2.9	0.945, 0.923	
3710	14:19:24.026	52:48:28.99	10.4/10.3 $^{+1.0}_{-1.0}$	-19.1	>1.2, >1.6	-5.2, -10.6	0.965, 0.996	F22, B22M
73150	14:19:26.780	52:54:16.61	10.6/10.4 $^{+0.8}_{-0.8}$	-19.1	>1.4, >1.8	-6.4, -11.8	0.973, 0.998	F22
20757	07:23:12.463	-73:28:01.71	10.7/12.8 $^{+0.6}_{-1.6}$	-17.9	>1.3, >0.9	1.6, -2.4	0.545, 0.899	
26598	07:22:50.553	-73:27:37.86	10.8/9.7 $^{+1.3}_{-1.6}$	-18.5	>1.0, >1.3	-3.2, -5.2	0.920, 0.966	
120880	14:20:10.558	52:59:39.51	10.8/10.4 $^{+0.5}_{-0.4}$	-19.4	>1.2, >1.0	-8.7, -6.8	0.983, 0.969	WA22, F22
6415	00:14:00.275	-30:21:25.90	10.8/10.6 $^{+0.6}_{-0.7}$	-19.1	>1.9, >1.6	-5.6, -5.4	0.975, 0.972	H22, B22
622_4	14:19:16.536	52:47:47.38	11.3/11.2 $^{+0.9}_{-1.1}$	-18.9	>1.0, >1.4	-4.3, -3.8	0.934, 0.910	
77241	14:19:41.462	52:54:41.51	11.3/11.2 $^{+0.7}_{-0.8}$	-19.3	>1.0, 1.1 \pm 1.8	-10.5, -6.9	0.995, 0.984	F22
33593_2	14:19:37.588	52:56:43.85	11.3/11.4 $^{+0.3}_{-0.4}$	-19.6	>1.4, >1.1	-4.0, -2.3	0.753, 0.721	F22
5268_2	14:19:19.678	52:53:32.14	11.4/11.3 $^{+0.6}_{-0.6}$	-19.2	0.9 \pm 0.9, 1.6 \pm 1.4	-2.8, -5.1	0.840, 0.959	
8347	07:22:56.351	-73:29:00.49	11.9/11.7 $^{+0.5}_{-0.5}$	-19.1	1.1 \pm 0.5, >1.4	-4.5, -8.0	0.898, 0.987	
26409_4	14:19:38.478	52:51:18.16	11.9/14.5 $^{+2.3}_{-2.3}$	-18.8	0.7 \pm 1.3, >0.9	-3.4, -3.9	0.914, 0.941	
10566	07:23:03.469	-73:28:46.97	12.0/13.7 $^{+0.9}_{-1.0}$	-19.7	>1.6, >1.7	-8.2, -5.9	0.991, 0.978	
27535_4	14:19:27.307	52:51:29.20	12.6/12.3 $^{+1.0}_{-1.0}$	-19.4	>1.9, >2.3	-6.5, -6.9	0.970, 0.987	
93316	14:19:39.481	52:56:34.96	16.4/16.3 $^{+0.3}_{-0.4}$	-21.3	1.7 \pm 0.1, 1.6 \pm 0.1	-8.7, -7.2	0.987, 0.962	H22, F22, B22, B22M, N22, Z22
Donnan et al. (2022, v1)								
28093	07:23:37.889	-73:27:21.87	9.2/9.0 $^{+1.2}_{-1.4}$	-18.9	>1.2, >1.5	-5.6, -6.0	0.973, 0.962	
26225	14:19:11.028	52:50:22.44	9.2/9.6 $^{+0.8}_{-0.7}$	-18.7	>1.2, >1.9	1.2, -1.8	0.562, 0.816	
78693	14:19:39.375	52:54:49.55	9.6/11.1 $^{+1.9}_{-1.5}$	-18.5	>0.9, >1.0	-3.2, -3.4	0.871, 0.873	
45704	14:19:28.719	52:51:36.87	10.0/10.9 $^{+2.2}_{-1.8}$	-18.6	>0.8, >1.0	-2.9, -3.4	0.860, 0.891	
30498	14:19:28.710	52:50:37.16	10.9/10.5 $^{+0.8}_{-0.9}$	-19.6	>1.5, 1.9 \pm 2.3	-3.6, -6.2	0.921, 0.979	F22
6486	07:22:53.246	-73:29:08.77	12.6/12.8 $^{+1.3}_{-1.2}$	-18.6	>1.2, >1.0	-2.8, -2.4	0.845, 0.879	
Labbé et al. (2022)								
2859	14:19:21.728	52:49:04.57	8.9/7.4 $^{+0.9}_{-0.9}$	-19.2	0.3 \pm 0.4, 0.9 \pm 0.3	-7.2, -5.3	0.996, 0.989	
Harikane et al. (2022a, v2)								
GL-z9-10	00:14:03.473	-30:19:00.89	8.7/10.8 $^{+1.5}_{-1.7}$	-18.2	>0.7, >1.4	-4.6, -5.1	0.949, 0.959	
GL-z9-13	00:13:57.453	-30:17:59.97	8.7/8.3 $^{+2.5}_{-1.4}$	-18.1	>1.5, >1.6	-3.0, -4.9	0.813, 0.942	
GL-z9-8	00:14:00.833	-30:21:29.77	9.1/11.4 $^{+1.0}_{-1.2}$	-18.1	>1.3, 1.1 \pm 1.1	0.6, -6.5	0.541, 0.975	
GL-z9-9	00:14:03.728	-30:21:03.49	9.3/10.6 $^{+2.8}_{-2.5}$	-18.1	>0.9, >0.2	-2.8, -0.7	0.915, 0.792	
Harikane et al. (2022a, v1)								
GL-z9-11	00:14:06.587	-30:20:56.08	8.7/8.5 $^{+0.9}_{-1.0}$	-18.4	>1.1, >1.4	-4.5, -6.8	0.929, 0.972	
CR6-z12-1	14:19:17.510	52:49:35.38	12.0/11.9 $^{+1.4}_{-1.3}$	-18.1	>1.2, >1.4	-3.4, -6.7	0.915, 0.981	
Whitler et al. (2022, v2)								
EGS-37135	14:19:58.650	52:59:21.80	8.9/9.2 $^{+0.1}_{-0.1}$	-20.3	1.9 \pm 0.7, 1.4 \pm 0.4	-15.1, -7.1	0.999, 0.970	F22, B22
EGS-7860	14:19:00.643	52:50:12.00	10.1/10.3 $^{+0.8}_{-0.7}$	-19.6	>1.8, >1.8	-7.8, -7.7	0.986, 0.990	B22M

* Same remarks apply to this table as Table 3

Table B2. Sample of $z \sim 10$, $z \sim 13$, and $z \sim 17$ candidate that we deem to be “solid” using our own photometry on our fiducial NIRC*am* reductions*

ID	RA	DEC	z_{phot}	M_{UV}	Break [mag]	$\Delta\chi^2$	$p(z > 5.5)$	Lit
Whitler et al. (2022, v1)								
EGS–38601	14:19:56.427	52:59:25.69	$8.8/8.2^{+0.3}_{-0.2}$	–20.3	$0.6 \pm 0.1, 0.8 \pm 0.1$	–5.9, –7.4	0.935, 0.980	
EGS–11330	14:19:35.255	52:50:56.47	$9.5/10.2^{+1.1}_{-1.0}$	–19.3	$>1.4, >1.8$	–1.8, –2.2	0.799, 0.867	
Finkelstein et al. (2022b)								
CEERS2_2274	14:19:23.077	52:53:38.41	$8.6/8.4^{+0.5}_{-0.5}$	–18.4	$0.7 \pm 1.5, 0.8 \pm 3.2$	–9.4, –4.0	0.997, 0.900	
CEERS1_5534	14:19:48.017	52:56:57.40	$8.6/8.5^{+0.5}_{-0.4}$	–19.6	$0.9 \pm 0.5, 1.0 \pm 0.8$	–10.4, –3.8	0.992, 0.958	
CEERS6_4012	14:19:33.148	52:51:32.37	$8.9/9.0^{+0.4}_{-0.4}$	–19.9	$1.1 \pm 0.8, 1.2 \pm 0.8$	–4.7, –1.2	0.901, 0.651	
CEERS1_1875	14:19:48.459	52:58:18.28	$8.9/9.6^{+1.1}_{-0.9}$	–20.4	$>1.4, >1.4$	–3.4, –0.3	0.904, 0.704	
CEERS1_3908	14:20:01.240	52:59:47.71	$9.0/9.8^{+0.9}_{-0.9}$	–20.2	$>1.6, >1.9$	–10.0, –5.2	0.993, 0.961	B22, B22M
CEERS6_7603	14:19:36.297	52:50:49.20	$11.3/11.6^{+1.1}_{-1.1}$	–19.0	$1.1 \pm 1.6, >1.0$	–3.9, –6.0	0.880, 0.948	D22
Yan et al. (2022)								
F150DB–026	07:23:23.735	–73:27:40.59	$11.4/10.5^{+0.8}_{-0.8}$	–19.4	$>1.1, >1.8$	–7.9, –3.7	0.989, 0.965	
F150DA–060	07:22:40.758	–73:28:23.75	$11.4/12.6^{+0.9}_{-0.9}$	–19.2	$>1.7, >1.2$	–5.3, 0.3	0.957, 0.550	
F150DB–013	07:23:05.525	–73:27:50.66	$11.4/13.1^{+1.1}_{-1.0}$	–20.1	$>0.9, >1.6$	–1.2, –3.5	0.616, 0.904	
F150DB–084	07:23:07.540	–73:26:23.79	$11.6/12.2^{+2.6}_{-2.4}$	–19.4	$0.8 \pm 2.5, >0.8$	–0.5, 0.2	0.764, 0.707	
F150DA–038	07:23:02.955	–73:28:46.16	$13.4/12.0^{+2.8}_{-2.8}$	–19.2	$>0.9, >0.5$	–1.1, –0.8	0.792, 0.719	
F150DA–008	07:22:52.747	–73:29:51.64	$13.4/12.5^{+3.1}_{-4.8}$	–20.1	$>0.4, >0.1$	–0.3, –0.5	0.763, 0.749	
F150DA–007	07:22:44.875	–73:29:53.68	$13.4/13.4^{+1.2}_{-1.2}$	–19.5	$>1.8, 1.0 \pm 1.0$	–2.2, –0.4	0.836, 0.612	
F200DA–089	07:22:32.427	–73:28:06.77	$14.2/14.8^{+4.2}_{-6.0}$	–19.0	$>0.7, >1.0$	–1.1, –1.4	0.751, 0.766	
F150DB–007	07:23:23.966	–73:27:58.78	$14.6/14.7^{+1.0}_{-1.0}$	–20.0	$1.1 \pm 1.9, >1.4$	–0.4, –1.3	0.783, 0.710	
F150DB–048	07:23:01.562	–73:27:18.02	$15.0/12.1^{+0.2}_{-0.4}$	–21.0	$1.5 \pm 0.3, 1.1 \pm 0.4$	–7.9, –1.1	0.969, 0.554	
F200DB–086	07:23:06.415	–73:27:19.85	$15.4/14.2^{+3.6}_{-2.7}$	–20.2	$>1.2, >2.0$	–0.4, –2.4	0.787, 0.915	
F200DB–015	07:23:07.672	–73:28:01.56	$16.0/18.4^{+1.0}_{-1.1}$	–19.4	$>1.6, >1.5$	–10.3, –6.2	0.997, 0.975	
F200DA–034	07:23:05.208	–73:29:13.37	$19.8/10.0^{+1.4}_{-1.3}$	–19.2	$0.5 \pm 1.0, >1.1$	0.2, –0.6	0.616, 0.817	
F200DA–098	07:22:34.793	–73:28:00.21	$19.8/15.3^{+1.3}_{-4.4}$	–19.4	$>1.1, >0.4$	0.6, –1.2	0.702, 0.817	
This Work (Fiducial Sample)								
GLASSPIJ–4003721456	00:14:00.378	–30:21:45.54	$9.2/9.2^{+0.8}_{-0.7}$	–19.2	$>1.6, >1.3$	–4.1, –4.4	0.953, 0.964	
This Work (Alternate Sample)								
CEERSJ–9494458188	14:19:49.446	52:58:18.89	$8.8/9.0^{+0.9}_{-0.5}$	–19.2	$1.2 \pm 1.8, 1.6 \pm 2.2$	–5.0, –9.4	0.913, 0.993	
GLASSPIJ–4016420474	00:14:01.649	–30:20:47.44	$9.6/9.6^{+0.4}_{-0.4}$	–18.9	>2.2	–6.0	0.954	
CEERSJ–9132749268	14:19:13.277	52:49:26.89	$9.7/9.7^{+0.7}_{-0.6}$	–19.0	>2.0	–4.9	0.962	
CEERSJ–9329250443	14:19:32.926	52:50:44.37	$10.1/10.1^{+0.6}_{-0.6}$	–19.3	$>1.6, >2.1$	0.4, –3.5	0.527, 0.947	
GLASSPIH–4015021230	00:14:01.507	–30:21:22.85	$13.3/11.3^{+3.0}_{-2.0}$	–18.9	$>0.9, >1.4$	–0.2, –6.3	0.741, 0.968	

* Same remarks apply to this table as Table 3

mag, than the median stack results in the “possible” category show, where the break only has an amplitude of ~ 1 –1.5 mag.

APPENDIX D: UV LF AT $Z \sim 8$

It is useful to test of our procedures for deriving the UV LF at high redshifts using *JWST* data to ensure we can arrive at reliable results.

To this end, we made use of our $z \sim 8$ F090W-dropout samples and the same methodology as we use for our $z \geq 8$ analyses to derive the UV LFs at $z \sim 8$. The results are presented in Figure D1 and in Tables 6–7, and it is clear that the results are consistent with what we derived earlier in Bouwens et al. (2021) on the basis of sensitive imaging observations with HST.

As such, we can conclude that our procedures should produce reliable UV LF results at $z \geq 8$, assuming we are able to identify significant samples at $z \geq 8$ which are largely free of contamination from lower-redshift interlopers.

APPENDIX E: STUDY-TO-STUDY SCATTER IN THE ASSESSMENT OF VARIOUS $Z \geq 9$ CANDIDATES

Ascertaining whether individual $z \geq 8$ candidates are at low or high-redshift can be challenging to answer in specific cases, due to uncertainties in both the photometry of individual sources and the optimal SED templates to utilize in performing the fits.

As an illustration of these uncertainties, Figure E1 shows a comparison of the $\Delta(\chi^2_{min, z > 5.5} - \chi^2_{min, z < 5.5})$ results obtained using our photometry on the GRIZLI reductions and those obtained using the PENCIL reductions. As a second illustration of the study-to-study differences, Figure E2 shows a comparison between the $\Delta(\chi^2_{min, z > 5.5} - \chi^2_{min, z < 5.5})$ results Harikane et al. (2022a) and the results we obtain using our GRIZLI reductions.

In both comparisons, there is clearly a significant amount of scatter in the assessments that are made about specific candidates.

Table B3. Sample of $z \sim 10$, $z \sim 13$, and $z \sim 17$ candidate that we deem to be “possible” using our own photometry on two separate reductions of the NIRCam data.*

ID	RA	DEC	z_{phot}	M_{UV}	Break [mag]	$\Delta\chi^2$	$p(z > 5.5)$	Lit
Castellano et al. (2022, v2)								
GHZ6	00:13:54.970	−30:18:53.68	$9.1/9.7^{+4.5}_{-2.0}$	−20.1	$0.9 \pm 1.0, > 1.0$	3.8, 1.4	0.063, 0.382	
GHZ5	00:13:58.661	−30:18:27.39	$9.2/7.2^{+1.9}_{-0.9}$	−20.2	$1.0 \pm 1.0, 1.6 \pm 1.0$	5.4, 6.2	0.116, 0.049	
Castellano et al. (2022, v1)								
GHZ6	00:13:57.689	−30:19:37.71	$9.1/11.2^{+4.8}_{-4.5}$	−19.4	$0.6 \pm 3.4, 1.1 \pm 1.9$	1.7, 18.2	0.394, 0.001	
Atek et al. (2022, v2)								
SMACS_z10d	07:22:46.695	−73:28:40.88	$9.3/10.8^{+0.6}_{-0.3}$	−19.8	$> 1.4, 0.9 \pm 1.2$	−1.4, 3.4	0.664, 0.129	
SMACS_z10e	07:22:45.296	−73:29:30.52	$10.9/10.3^{+1.3}_{-2.5}$	−18.9	$> 0.9, > 1.4$	2.0, 1.2	0.328, 0.461	
SMACS_z11a	07:22:39.500	−73:29:40.20	$11.1/10.6^{+0.7}_{-0.5}$	−18.6	$> 1.5, 1.0 \pm 0.9$	−2.0, 2.4	0.714, 0.230	
SMACS_z12a	07:22:47.373	−73:30:01.76	$12.2/12.7^{+2.1}_{-1.2}$	−19.8	$1.0 \pm 0.9, 1.2 \pm 2.3$	2.6, 0.9	0.283, 0.556	
SMACS_z16a	07:23:26.387	−73:28:04.55	$15.9/10.6^{+0.6}_{-1.1}$	−20.6	$> 1.1, > 1.1$	1.7, 0.3	0.311, 0.523	
Atek et al. (2022, v1)								
SMACS_z10f	07:22:57.297	−73:29:16.49	$10.5/8.9^{+1.8}_{-0.9}$	−19.2	$1.5 \pm 2.1, 1.0 \pm 0.4$	0.8, 1.8	0.525, 0.201	
SMACS_z11b	07:22:53.835	−73:28:23.28	$11.2/9.7^{+1.2}_{-2.0}$	−22.4	1.7 ± 1.3	1.7	0.305	
SMACS_z11c	07:23:01.597	−73:26:54.89	$11.2/10.9^{+1.0}_{-1.0}$	−19.6	$> 0.9, > 1.8$	−0.8, −0.1	0.530, 0.540	
SMACS_z11d	07:22:36.750	−73:28:09.17	$11.3/10.7^{+0.5}_{-0.3}$	−21.8	$1.9 \pm 2.6, 0.7 \pm 0.2$	0.3, 5.7	0.560, 0.029	
SMACS_z11e	07:22:49.255	−73:27:44.56	$11.5/12.3^{+2.3}_{-1.6}$	−19.2	$1.0 \pm 1.7, 1.2 \pm 1.4$	−1.0, 1.8	0.675, 0.621	Y22
Donnan et al. (2022, v2)								
3398	07:22:35.369	−73:29:38.62	$9.7/8.2^{+1.4}_{-1.3}$	−18.2	$> 1.4, > 1.3$	1.4, −0.5	0.608, 0.717	
4063	07:22:52.307	−73:29:32.38	$10.4/8.1^{+1.7}_{-1.4}$	−18.0	$> 1.0, > 1.2$	3.4, 1.4	0.411, 0.526	
6647	14:19:14.663	52:48:49.77	$10.4/9.8^{+1.6}_{-1.3}$	−18.9	$> 1.1, > 1.4$	1.8, −0.5	0.295, 0.528	
21071_2	14:19:36.716	52:55:22.66	$10.7/10.2^{+1.0}_{-1.2}$	−19.3	$0.9 \pm 1.2, 1.0 \pm 1.7$	5.8, 2.8	0.112, 0.200	
61486	14:19:23.727	52:53:00.98	$11.2/10.5^{+2.8}_{-2.0}$	−19.6	$> 1.7, > 1.6$	2.0, −0.9	0.510, 0.683	
1566	07:22:39.183	−73:30:00.55	$12.3/10.0^{+2.0}_{-2.6}$	−18.8	$1.0 \pm 1.1, 1.1 \pm 2.1$	2.5, 0.8	0.352, 0.561	
Donnan et al. (2022, v1)								
2873	14:19:21.556	52:48:20.82	$9.0/9.6^{+1.2}_{-1.2}$	−18.8	$> 1.2, 1.9 \pm 1.8$	1.3, 3.5	0.468, 0.326	
9544	07:22:38.627	−73:28:46.53	$9.1/9.0^{+1.4}_{-2.2}$	−19.0	$1.2 \pm 0.5, 1.9 \pm 1.2$	4.1, 1.1	0.181, 0.536	
111451	14:19:50.598	52:58:48.64	$9.1/9.2^{+1.0}_{-0.8}$	−18.9	$> 1.5, 0.8 \pm 1.2$	1.1, 1.4	0.568, 0.433	
106309	14:19:52.004	52:58:05.85	$9.2/9.0^{+0.8}_{-0.6}$	−18.8	$1.8 \pm 2.3, > 1.5$	0.3, 0.2	0.718, 0.631	F22
110933	14:20:00.345	52:58:44.25	$9.3/8.9^{+1.3}_{-1.3}$	−18.7	$> 1.2, 1.1 \pm 1.5$	3.9, 6.0	0.356, 0.204	
108408	14:19:46.666	52:58:21.42	$9.3/9.7^{+0.9}_{-0.7}$	−19.1	$> 1.7, > 1.7$	1.8, 1.7	0.355, 0.483	
107364	14:19:49.568	52:58:13.33	$10.2/8.6^{+0.5}_{-0.4}$	−19.1	$0.8 \pm 0.6, 0.8 \pm 0.8$	7.8, 5.3	0.027, 0.055	
20311	14:18:59.916	52:49:56.40	$10.8/10.7^{+0.6}_{-0.8}$	−19.3	$1.8 \pm 1.7, 1.2 \pm 0.5$	−1.1, 7.3	0.727, 0.030	
78598	14:19:30.185	52:54:48.79	$11.0/12.0^{+1.7}_{-0.8}$	−19.5	$1.1 \pm 2.9, > 1.1$	2.4, 3.1	0.418, 0.279	
35470	07:23:02.966	−73:26:47.49	$12.0/12.4^{+2.1}_{-1.2}$	−19.2	$> 1.4, > 1.8$	−0.1, 0.8	0.581, 0.567	
21901	07:22:46.756	−73:27:49.43	$12.2/12.4^{+1.0}_{-0.8}$	−19.0	$1.5 \pm 1.5, > 1.9$	1.2, 0.4	0.587, 0.697	
40079	07:23:13.894	−73:26:05.07	$14.3/12.3^{+2.6}_{-1.0}$	−19.6	$> 1.1, > 0.8$	3.2, −0.1	0.354, 0.595	
Harikane et al. (2022a, v2)								
GL−z9−5	00:14:03.114	−30:22:26.29	$8.7/8.6^{+0.9}_{-0.8}$	−18.8	$> 1.7, > 1.0$	−0.4, 0.5	0.728, 0.471	
GL−z9−3	00:14:00.093	−30:19:06.89	$8.9/5.7^{+0.5}_{-0.3}$	−18.8	$0.9 \pm 2.4, 1.2 \pm 0.1$	−0.1, −0.1	0.520, 0.478	
GL−z9−6	00:14:04.398	−30:20:39.78	$9.0/8.8^{+1.1}_{-0.4}$	−18.9	$> 2.0, > 2.2$	3.1, −5.8	0.286, 0.969	B22M
GL−z9−12	00:14:06.869	−30:22:01.96	$9.1/7.3^{+1.0}_{-0.8}$	−18.2	$1.6 \pm 2.0, > 0.2$	0.7, 0.5	0.507, 0.577	
GL−z9−11	00:14:02.489	−30:22:00.91	$9.9/10.3^{+3.3}_{-2.6}$	−18.6	$0.6 \pm 2.1, > 0.5$	1.9, 0.4	0.308, 0.637	
GL−z9−7	00:14:02.533	−30:21:57.09	$10.3/10.7^{+4.3}_{-2.2}$	−18.2	$1.2 \pm 1.1, > 1.5$	1.4, −2.1	0.479, 0.845	
CR2−z12−3	14:19:41.606	52:55:07.60	$11.7/12.0^{+1.7}_{-1.4}$	−19.2	$> 0.6, 0.6 \pm 1.1$	−1.1, 0.4	0.781, 0.607	
CR2−z12−2	14:19:42.567	52:54:42.03	$12.0/10.7^{+1.7}_{-2.2}$	−19.0	$1.1 \pm 1.8, > 1.3$	5.7, 3.1	0.241, 0.429	
CR2−z12−4	14:19:24.858	52:53:13.93	$12.1/11.3^{+3.2}_{-2.2}$	−19.0	$> 0.3, 0.4 \pm 1.0$	−0.7, 0.6	0.733, 0.649	
SM−z12−1	07:22:32.471	−73:28:33.18	$12.5/10.2^{+0.9}_{-1.4}$	−18.5	$> 1.3, > 1.2$	1.7, 0.0	0.408, 0.744	Y22
Harikane et al. (2022a, v1)								
GL−z9−5	00:13:58.209	−30:21:34.29	$9.2/9.0^{+1.7}_{-0.2}$	−18.7	$> 1.5, 1.5 \pm 1.6$	15.2, 19.1	0.001, 0.000	
GL−z9−15	00:14:00.487	−30:21:24.49	$9.8/8.9^{+2.5}_{-2.2}$	−18.1	$> 0.8, > 1.1$	2.0, 0.9	0.452, 0.562	
SM−z12−1	07:22:58.264	−73:28:32.99	$11.5/13.0^{+1.5}_{-1.3}$	−18.0	$> 1.1, 1.2 \pm 2.7$	−1.7, −0.6	0.793, 0.647	
CR2−z12−2	14:19:24.237	52:54:24.81	$11.6/6.8^{+1.0}_{-0.5}$	−19.4	$0.9 \pm 1.8, > 0.6$	−0.7, 4.5	0.692, 0.255	
CR3−z12−1	14:19:11.106	52:49:33.70	$11.7/10.1^{+1.8}_{-1.3}$	−18.3	$> 1.0, > 1.1$	−1.5, 0.3	0.772, 0.522	H22
CR2−z12−3	14:19:30.405	52:52:51.35	$12.1/12.7^{+1.9}_{-1.4}$	−19.2	$> 0.6, > 1.0$	1.3, −0.4	0.524, 0.674	

Table B4. Sample of $z \sim 10$, $z \sim 13$, and $z \sim 17$ candidate that we deem to be “possible” using our own photometry on two separate reductions of the NIRCam data.*

ID	RA	DEC	z_{phot}	M_{UV}	Break [mag]	$\Delta\chi^2$	$p(z > 5.5)$	Lit
Whitler et al. (2022, v2)								
EGS-34362	14:20:03.000	53:00:04.88	9.2/9.1 ^{+0.4} _{-0.3}	-20.2	1.4±0.8	5.5	0.098	
EGS-14506	14:19:13.719	52:51:44.49	10.7/9.2 ^{+1.1} _{-0.7}	-20.2	1.0±0.6, 0.9±0.3	2.3, 5.5	0.331, 0.051	
Whitler et al. (2022, v1)								
EGS-36603	14:20:09.204	52:59:54.73	9.3/7.9 ^{+1.0} _{-1.0}	-19.9	0.7±1.5	-1.4	0.731	
EGS-42956	14:19:48.045	52:58:27.52	10.4/9.2 ^{+1.5} _{-0.9}	-19.9	1.3±1.6, 1.5±2.3	1.2, 0.8	0.396, 0.421	
Finkelstein et al. (2022b)								
CEERS1_7227	14:20:08.996	52:59:57.79	11.2/10.9 ^{+0.7} _{-0.6}	-19.2	0.8±2.3	0.6	0.335	
CEERS1_1730	14:20:02.397	53:00:49.09	13.4/12.7 ^{+1.2} _{-1.0}	-20.2	1.0±0.9	1.6	0.572	
Yan et al. (2022)								
F150DB-C_4	07:23:25.966	-73:26:39.89	10.4/9.8 ^{+2.1} _{-1.2}	-19.9	1.8±0.1, 1.8±0.2	3.8, 4.4	0.215, 0.151	
F150DB-040	07:23:11.937	-73:27:24.93	10.8/7.7 ^{+3.4} _{-1.5}	-20.5	0.5±1.6, 0.9±1.6	5.3, 6.2	0.065, 0.069	
F150DA-026	07:22:46.013	-73:29:08.12	11.0/8.2 ^{+3.0} _{-1.8}	-19.1	0.2±0.8, 0.9±3.2	1.1, 2.3	0.258, 0.380	
F150DA-036	07:23:00.669	-73:28:48.71	11.0/11.2 ^{+0.7} _{-0.4}	-19.2	0.9±0.4, 0.8±1.1	3.0, 3.6	0.219, 0.205	
F150DA-020	07:22:55.876	-73:29:17.45	11.2/7.9 ^{+3.7} _{-1.7}	-19.3	0.7±1.0, >0.8	1.6, 1.6	0.179, 0.399	
F150DA-005	07:22:41.008	-73:29:54.98	11.2/9.8 ^{+1.9} _{-1.0}	-19.4	0.7±0.3, 0.6±0.4	6.5, 4.8	0.029, 0.041	
F150DA-062	07:22:54.222	-73:28:23.56	11.4/8.6 ^{+2.7} _{-1.9}	-19.9	>0.9, 0.9±2.8	1.4, 0.6	0.437, 0.514	
F150DA-057	07:22:58.715	-73:28:28.37	11.4/9.9 ^{+1.6} _{-1.3}	-20.9	1.0±1.4, 1.0±1.0	8.4, 9.2	0.019, 0.014	
F150DA-066	07:22:39.616	-73:28:12.16	11.4/10.5 ^{+0.9} _{-1.1}	-19.8	1.0±0.3, 0.9±1.2	7.0, 6.4	0.080, 0.135	
F150DB-075	07:23:02.229	-73:26:41.51	11.4/10.8 ^{+0.8} _{-0.4}	-21.2	>1.5, >2.1	5.5, 4.0	0.076, 0.110	
F150DA-054	07:22:38.904	-73:28:30.84	11.4/11.1 ^{+0.8} _{-0.6}	-19.2	0.9±0.4, 1.4±1.8	0.2, -2.2	0.481, 0.826	
F150DB-090	07:23:26.236	-73:26:13.82	11.4/11.3 ^{+0.3} _{-0.2}	-21.6	1.2±0.6, 1.3±0.7	5.3, 7.0	0.026, 0.011	
F150DA-052	07:22:26.930	-73:28:33.80	11.4/12.2 ^{+2.1} _{-1.2}	-19.3	1.0±1.2	-0.4	0.591	
F150DA-031	07:22:40.648	-73:29:00.50	11.4/13.1 ^{+1.5} _{-1.4}	-19.6	1.1±0.7, 1.1±1.0	1.5, -1.3	0.632, 0.664	
F150DB-054	07:23:12.503	-73:27:10.74	11.4/15.0 ^{+2.3} _{-1.4}	-19.3	1.0±1.0, 0.7±0.5	3.4, 7.4	0.265, 0.026	
F150DB-076	07:23:29.414	-73:26:39.77	11.6/6.0 ^{+0.4} _{-0.1}	-19.6	0.5±0.5, 0.7±0.5	8.3, 8.5	0.008, 0.006	
F150DB-050	07:23:24.576	-73:27:15.06	11.6/6.7 ^{+0.1} _{-0.2}	-19.5	0.8±0.7, 1.4±1.4	14.5, 18.3	0.001, 0.000	
F150DB-044	07:23:39.315	-73:27:22.28	11.6/7.0 ^{+0.0} _{-0.7}	-19.6	0.8±0.3, 0.4±0.3	20.1, 20.2	0.000, 0.000	
F150DB-095	07:23:24.766	-73:26:01.29	11.6/9.3 ^{+2.1} _{-2.4}	-19.4	1.4±2.5, 1.7±1.0	3.9, 2.1	0.156, 0.138	
F150DB-011	07:23:27.382	-73:27:58.03	11.6/10.8 ^{+1.0} _{-0.9}	-19.5	0.7±0.3, 0.7±0.5	7.4, 7.4	0.030, 0.041	
F150DA-019	07:22:39.395	-73:29:20.47	11.6/11.1 ^{+0.6} _{-0.7}	-19.4	>0.8, >1.2	4.4, 1.9	0.165, 0.400	
F150DB-082	07:23:22.754	-73:26:25.63	11.6/11.4 ^{+0.8} _{-0.7}	-20.0	>1.0, >1.7	1.9, -2.6	0.296, 0.859	
F150DB-088	07:23:14.037	-73:26:17.28	11.6/11.5 ^{+0.3} _{-0.1}	-19.7	1.1±0.9, 1.1±0.2	10.4, 10.5	0.003, 0.004	
F150DB-031	07:23:21.438	-73:27:36.32	11.6/13.1 ^{+1.8} _{-1.5}	-19.2	>1.2, >1.7	-0.3, 1.0	0.649, 0.443	
F150DB-021	07:23:12.643	-73:27:45.24	11.8/6.2 ^{+0.5} _{-0.0}	-20.5	0.5±0.3, 0.3±0.2	0.6, 0.8	0.265, 0.204	
F150DA-078	07:22:49.244	-73:27:49.86	11.8/8.1 ^{+2.0} _{-1.5}	-19.8	1.1±1.8, 1.7±2.6	0.7, 2.1	0.447, 0.158	
F150DB-069	07:23:04.258	-73:26:54.20	11.8/11.2 ^{+0.6} _{-0.7}	-19.4	1.0±0.6, >1.8	1.6, -2.2	0.468, 0.784	
F150DA-015	07:22:44.735	-73:29:26.86	11.8/11.5 ^{+0.4} _{-0.5}	-19.3	>0.9, 0.7±0.5	-1.0, 3.7	0.574, 0.143	
F150DA-083	07:22:42.714	-73:27:32.28	11.8/13.2 ^{+3.4} _{-6.3}	-20.6	1.0±0.8, >0.9	2.6, 1.7	0.358, 0.351	
F150DA-010	07:22:40.082	-73:29:46.12	12.8/10.8 ^{+1.1} _{-0.1}	-19.4	0.7±0.4, 0.3±0.7	4.1, 5.3	0.107, 0.064	
F150DA-058	07:22:48.273	-73:28:27.35	13.4/8.6 ^{+3.1} _{-2.1}	-20.0	>0.7, >0.8	2.0, 1.7	0.266, 0.334	
F150DA-075	07:22:38.343	-73:27:57.09	13.4/9.4 ^{+1.9} _{-2.0}	-19.8	0.5±0.7, >1.0	-0.2, 2.0	0.751, 0.535	
F150DA-050	07:22:44.994	-73:28:36.88	13.4/10.0 ^{+1.1} _{-1.9}	-19.9	>1.5, 0.8±0.4	-0.6, 2.1	0.500, 0.276	
F150DB-079	07:23:13.156	-73:26:29.64	13.8/12.5 ^{+1.8} _{-1.9}	-19.8	1.3±2.2, >1.5	-0.1, 0.1	0.639, 0.595	
F150DB-004	07:23:14.299	-73:28:06.75	14.0/11.7 ^{+2.5} _{-0.5}	-19.6	0.9±0.9, 0.9±0.9	8.6, 4.2	0.017, 0.232	
F150DB-033	07:23:30.548	-73:27:33.10	14.8/10.5 ^{+0.9} _{-0.2}	-19.9	>1.4, >1.5	3.5, 6.1	0.109, 0.088	
F150DB-052	07:23:28.136	-73:27:13.86	15.0/11.5 ^{+0.5} _{-0.3}	-20.5	0.9±0.3, >1.5	3.4, 3.4	0.133, 0.283	
F150DB-058	07:23:24.096	-73:27:09.81	15.2/8.8 ^{+1.1} _{-1.2}	-20.6	>0.9, >1.6	6.7, 0.9	0.127, 0.692	
F200DA-056	07:22:37.024	-73:28:41.57	15.6/6.2 ^{+3.0} _{-0.1}	-19.3	0.9±0.4, 1.0±0.6	4.5, 2.5	0.028, 0.052	
F200DB-109	07:23:37.033	-73:27:12.22	15.8/7.2 ^{+2.7} _{-0.9}	-19.2	0.3±1.6, 0.2±0.9	1.0, 2.9	0.397, 0.188	
F200DB-181	07:23:12.615	-73:26:31.71	15.8/14.5 ^{+1.2} _{-1.4}	-20.5	>0.9, >1.1	-1.9, 2.7	0.790, 0.290	
F200DA-061	07:22:31.695	-73:28:38.65	15.8/16.6 ^{+1.8} _{-1.1}	-19.6	1.4±1.2, 1.1±0.9	2.1, 0.5	0.431, 0.589	
F150DB-041	07:23:06.626	-73:27:25.43	16.0/11.6 ^{+0.3} _{-0.3}	-20.0	>1.1, >1.8	0.6, 3.2	0.546, 0.214	
F200DB-159	07:23:25.344	-73:26:46.02	16.0/13.2 ^{+4.8} _{-5.6}	-19.3	>1.1, >1.5	2.2, -0.7	0.512, 0.782	
F200DB-175	07:23:11.086	-73:26:38.01	16.2/12.8 ^{+1.3} _{-1.3}	-19.9	>1.6, >1.6	2.2, 1.8	0.387, 0.345	
F200DA-040	07:23:03.926	-73:29:06.14	20.0/9.2 ^{+1.8} _{-2.1}	-19.5	>0.7, 0.7±0.6	0.8, 1.1	0.532, 0.691	
F200DB-045	07:23:22.766	-73:27:39.69	20.4/14.2 ^{+3.7} _{-0.8}	-20.3	1.4±1.1, >1.3	0.4, 0.2	0.527, 0.518	
F200DA-006	07:22:40.349	-73:30:10.33	20.6/9.2 ^{+3.0} _{-2.5}	-19.6	0.6±0.3, >0.9	1.0, 1.9	0.336, 0.419	

* Same remarks apply to this table as Table 3

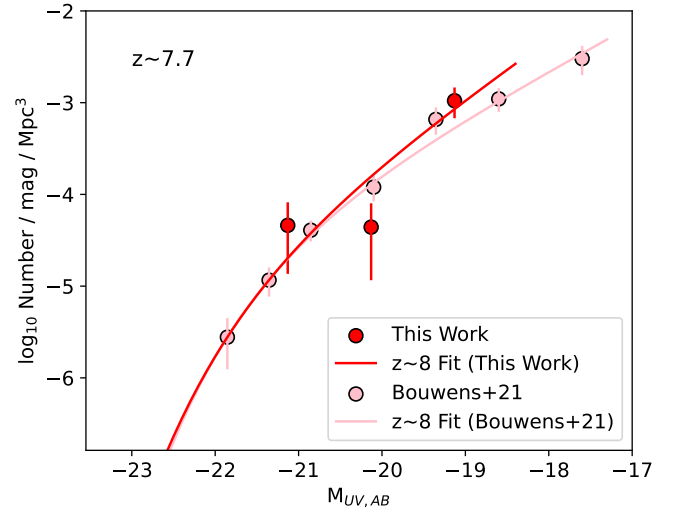
Table B5. Sample of $z \sim 10$, $z \sim 13$, and $z \sim 17$ candidate that we deem to be “possible” using our own photometry on two separate reductions of the NIRCcam data.*

ID	RA	DEC	z_{phot}	M_{UV}	Break [mag]	$\Delta\chi^2$	$p(z > 5.5)$	Lit
This Work (Fiducial Sample)								
CEERSJ-9345150450	14:19:34.513	52:50:45.08	9.2/9.2 $^{+0.8}_{-0.6}$	-19.5	1.5 \pm 1.0, 1.0 \pm 0.4	-10.5, 2.0	0.997, 0.424	
CEERSJ-9203050435	14:19:20.301	52:50:43.60	9.8/9.8 $^{+0.8}_{-0.7}$	-19.0	>1.7, 0.8 \pm 0.4	-8.9, 6.9	0.989, 0.044	
CEERSJ-9149352106	14:19:14.931	52:52:10.66	10.0/10.0 $^{+0.7}_{-0.7}$	-19.5	1.8 \pm 2.1, 1.1 \pm 0.5	-4.7, 2.7	0.956, 0.286	
CEERSJ-9026550577	14:19:02.650	52:50:57.75	11.2/11.3 $^{+0.4}_{-0.5}$	-18.9	>1.5, 0.9 \pm 0.4	-6.9, 13.3	0.983, 0.002	
This Work (Alternate Sample)								
GLASSP1J-4045920571	00:14:04.599	-30:20:57.10	9.4/8.0 $^{+1.0}_{-1.2}$	-19.2	>1.9, >2.3	1.4, -3.4	0.420, 0.885	
CEERSJ-9320850526	14:19:32.076	52:50:52.65	9.6/8.1 $^{+1.2}_{-1.0}$	-19.4	1.2 \pm 1.2, >2.3	1.8, -3.4	0.387, 0.930	
CEERSH-9220551139	14:19:22.049	52:51:13.94	13.5/12.2 $^{+1.5}_{-1.0}$	-19.5	>1.5, >1.9	2.5, -4.9	0.237, 0.971	

* Same remarks apply to this table as Table 3

Table C1. Median stack results for $z \geq 8$ candidates from the literature which we segregate into the “robust,” “solid,” and “possible” categories based on our own photometry and SED fits.

Band	Median Flux (nJy)		
	“Robust”	“Solid”	“Possible”
$z=8.5-11.5$			
F435W+F475W	-0 $^{+1}_{-1}$	-1 $^{+2}_{-3}$	2 $^{+2}_{-1}$
F606W+F775W+F814W	-0 $^{+1}_{-1}$	0 $^{+1}_{-1}$	2 $^{+2}_{-1}$
F090W	-1 $^{+1}_{-2}$	-3 $^{+3}_{-6}$	5 $^{+3}_{-2}$
F115W	7 $^{+4}_{-4}$	0 $^{+1}_{-1}$	5 $^{+3}_{-2}$
F125W+F140W	9 $^{+5}_{-4}$	4 $^{+5}_{-3}$	12 $^{+9}_{-6}$
F160W	22 $^{+8}_{-7}$	32 $^{+11}_{-10}$	20 $^{+9}_{-9}$
F150W	21 $^{+7}_{-6}$	32 $^{+7}_{-6}$	29 $^{+5}_{-5}$
F200W	20 $^{+7}_{-6}$	35 $^{+7}_{-7}$	31 $^{+5}_{-5}$
F277W	22 $^{+7}_{-6}$	33 $^{+6}_{-6}$	33 $^{+6}_{-6}$
F356W	28 $^{+7}_{-6}$	31 $^{+6}_{-6}$	37 $^{+5}_{-6}$
F444W	53 $^{+14}_{-14}$	38 $^{+8}_{-8}$	33 $^{+6}_{-5}$
$z=11.5-15.0$			
F435W+F475W	11 $^{+8}_{-8}$	-22 $^{+19}_{-18}$	-0 $^{+4}_{-3}$
F606W+F775W+F814W	-0 $^{+1}_{-2}$	11 $^{+7}_{-7}$	2 $^{+3}_{-1}$
F090W	0 $^{+1}_{-1}$	-0 $^{+2}_{-3}$	3 $^{+3}_{-3}$
F115W	-2 $^{+3}_{-4}$	-5 $^{+4}_{-3}$	7 $^{+3}_{-3}$
F125W+F140W	-19 $^{+11}_{-19}$	69 $^{+56}_{-48}$	2 $^{+8}_{-5}$
F160W	68 $^{+50}_{-51}$	18 $^{+16}_{-15}$	26 $^{+20}_{-17}$
F150W	4 $^{+6}_{-5}$	6 $^{+3}_{-3}$	14 $^{+4}_{-4}$
F200W	41 $^{+20}_{-19}$	46 $^{+26}_{-25}$	36 $^{+8}_{-7}$
F277W	39 $^{+17}_{-18}$	43 $^{+24}_{-23}$	37 $^{+8}_{-8}$
F356W	33 $^{+13}_{-15}$	33 $^{+18}_{-17}$	34 $^{+7}_{-7}$
F444W	37 $^{+17}_{-17}$	24 $^{+23}_{-20}$	29 $^{+7}_{-6}$
$z=15.0-20.0$			
F435W+F475W	—	-5 $^{+2}_{-47}$	0 $^{+14}_{-6}$
F606W+F775W+F814W	—	0 $^{+1}_{-2}$	1 $^{+4}_{-4}$
F090W	—	-13 $^{+6}_{-3}$	7 $^{+6}_{-4}$
F115W	—	-3 $^{+2}_{-1}$	4 $^{+10}_{-4}$
F125W+F140W	—	-1 $^{+4}_{-4}$	0 $^{+12}_{-9}$
F160W	—	5 $^{+66}_{-7}$	-29 $^{+19}_{-19}$
F150W	—	2 $^{+2}_{-2}$	14 $^{+9}_{-9}$
F200W	—	8 $^{+8}_{-8}$	20 $^{+11}_{-9}$
F277W	—	40 $^{+21}_{-21}$	41 $^{+13}_{-13}$
F356W	—	34 $^{+18}_{-17}$	33 $^{+11}_{-11}$
F444W	—	35 $^{+18}_{-18}$	27 $^{+11}_{-10}$

**Figure D1.** Determination of the UV LF at $z \sim 8$ (solid red circles) leveraging the new *JWST* observations over the three of the most studied early NIRCcam observations with *JWST*.

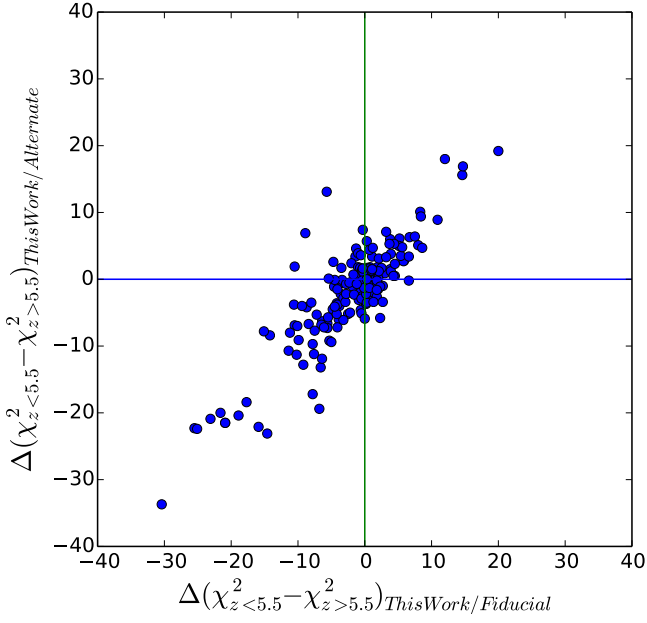


Figure E1. Difference between the minimum χ^2 achieved with $z > 5.5$ SED fits to specific sources and that obtained with $z < 5.5$ SED fits. $\Delta\chi^2$ values less than -9 or -4 tend to indicate sources are at $z > 5.5$ at high confidence. We note that there is nevertheless a substantial dispersion in the derived $\Delta\chi^2$ values depending on the reductions. If the uncertainties are similar in various literature studies, it could point to there being a significant amount of contamination and incompleteness in existing $z > 5.5$ selections.

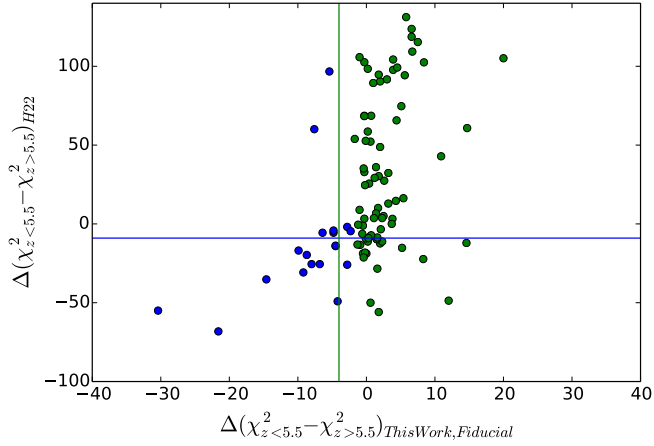


Figure E2. Similar to Figure E1 but comparing the source-by-source results of Harikane et al. (2022a) with those we obtain using our fiducial reductions from GRIZLI. Sources shown in blue are included in our fiducial sample while those shown in green are not. Note that the substantial dispersion in the derived $\Delta\chi^2$ values depending on the analysis.